Graduation Project

Modelling and sizing of post-processing equipment for wet hydrogen from alkaline electrolysis

Almas Mardanov

Delft University of Technology

Modelling and sizing of post-processing equipment for wet hydrogen from alkaline electrolysis

by

Almas Mardanov

Student Name	Student Number
Mardanov	4788303

TU Delft supervisor:	Dr.Ir.M.Ramdin
XINTC B.V. supervisor:	Dr.A.Rahbari
Project duration:	October 10, 2022 – August 31, 2023
Faculty:	Faculty of Mechanical, Maritime and Materials Engineering, TU Delft

Abstract

The increasing adoption of hydrogen in industrial applications is driven by its potential to decarbonize various industries. Among the various methods of hydrogen production, water electrolysis is considered one of the environmentally friendliest options. However, hydrogen produced from water electrolysis contains impurities such as oxygen and water vapour, and the required level of purity varies depending on the specific industrial application.

To address this issue, catalytic recombination of hydrogen and oxygen into water is selected as a method for oxygen removal due to its high efficacy in completely converting oxygen. Subsequently, hydrogen drying is achieved using Pressure Swing Adsorption (PSA) following the catalytic recombination process. This thesis work primarily focuses on the modelling and sizing of adsorption columns within the PSA system. One-dimensional dynamic models describing the pressurization, adsorption, depressurization, and desorption steps of PSA are mathematically derived and developed in Python. The adsorption modelling approach is validated using experimental data from a scientific paper. Insightful information was obtained during the model validation process, shedding light on the consequences of the assumptions made to simplify the energy balance, as well as revealing the decrease in adsorption capacity during the pressurization process.

The PSA system is designed to process 400 kg of hydrogen per day with the aim of reducing the water vapour content below 5 ppm. While pressure plays a central role in PSA control, it has been discovered that the primary design challenge relates to temperature control within the operating range. Therefore, adsorption column sizing is optimized, taking into account PSA performance and required energy input. A sensitivity analysis is conducted to identify the optimal adsorbent, considering zeolite 3A and silica gel. Based on the results, a column length of 2 meters and a diameter of 0.0914 meters are considered optimal for zeolite-packed adsorption columns, resulting in a productivity of 35.62 mol/hr/kg and requiring 50.21 kJ during the desorption step. The optimal size for silica gel-packed adsorption columns has not been determined due to a significant temperature drop during desorption, which could risk ice formation and subsequent flow blockage. Nevertheless, silica gel, with its higher adsorption capacity leading to a longer adsorption step, remains a viable option from an operational perspective and should not be disregarded as a potential choice.

Contents

List of Figures

List of Tables

Nomenclature

Abbreviations

Abbreviation	Definition
AEM	Anion exchange membrane electrolyser
AWE	Alkaline water electrolyser
IAST	Ideal adsorbed solution theory
ISO	International Standard Organization
LDF	Linear driving force
ODE	Ordinary differential equation
PDE	Partial differential equation
PEM	Proton exchange membrane electrolyser
PSA	Pressure Swing Adsorption
TSA	Temperature swing adsorption
VEMC	Viral excess mixing coefficient
VPSA	Vacuum pressure swing adsorption
VSA	Vacuum swing adsorption

Symbols

Symbol	Definition	Unit
c_i	Concentration of the component i	[mol/m^3]
u	Interstitial velocity	[m/s]
u_s	Superficial velocity	[m/s]
ϵ	Bed porosity	
ϵ_m	Mean bed porosity	
D_L	Axial dispersion coefficient	[m^2/s]
D_m	Molecular diffusion	[m^2/s]
C_{ps}	Specific heat capacity of the adsorbent	[J/kgK]
C_{pg}	Specific heat capacity of the gas	[J/kgK]
C_{pq}	Specific heat capacity of the wall	[J/kgK]
q_i	Loading of component i	[mol/kg]
q_i^{eq}	Equilibrium loading of component i	[mol/kg]
P	Pressure	[bar]
$\dot{q}_{\text{cond}}$	Conductive heat flux	[W/m^2]
$\dot{q}_{\text{conv}}$	Convective heat flux	[W/m^2]
$\dot{q}_{\text{source}}$	Heat source	[W/m^3]
T	Temperature	[K]
T_f	Fluid temperature	[K]
T_s	Adsorbent temperature	[K]
T_w	Adsorption wall column temperature	[K]
k_{eff}	Effective thermal conductivity of the bed	[W/mK]
h_f	Convective heat transfer from solid to fluid	[W/m^{2}K]
h_w	Convective heat transfer from fluid to wall	[W/m^{2}K]
h_∞	Convective heat transfer from wall to environment	[W/m^{2}K]
d_{in}	Inner diameter of adsorption column	[m]
d_{out}	Outer diameter of adsorption column	[m]

Symbol	Definition	Unit
d_p	Adsorbent particle diameter	[m]
t_w	Wall thickness	[m]
ΔH	Heat of adsorption	[J/mol]
k_{LDF}	Linear driving force coefficient	[1/s]
$\dot{m}$	Mass flow rate	[kg/s]
$\dot{m}_{\text{feed}}$	Feed mass flow rate	[kg/s]
A_c	Cross section area	[m^2]
A_{void}	Void area	[m^2]
A_{void}	Void area	[m^2]
A_s	Solid area	[m^2]
$A_{\text{wall,c}}$	Adsorption column wall cross section area	[m^2]
$A_{\text{wall}}^{\text{in}}$	Adsorption column inner wall surface area	[m^2]
$A_{\text{wall}}^{\text{out}}$	Adsorption column outer wall surface area	[m^2]
K	Permeability	[m^2]
V_{bed}	Bed volume	[m^3]
V_{void}	Void volume	[m^3]
V_s	Adsorbent volume	[m^3]
PE	Potential energy	[J]
KE	Kinetic energy	[J]
U_f	Fluid internal energy	[J]
U_s	Adsorbent internal energy	[J]
U_w	Wall internal energy	[J]
Nu	Nusselt number	
Pe	Peclet number	
Re	Reynolds number	
Sc	Schmidt number	
ρ_s	Adsorbent density	[kg/m^3]
ρ_f	Fluid density	[kg/m^3]
ρ_w	Wall density	[kg/m^3]
ρ_{feed}	Feed density	[kg/m^3]
μ	Dynamic viscosity	[Pa · s]

1

Introduction

1.1. Motivation

The part of the incident short-wave solar radiation (0.2-4 μm) is consumed to heat the Earth's surface and the heated Earth's surface emits long-wave radiation (4-100 μm) which is partially adsorbed by greenhouse gases, mainly CO_2, CH_4 and N_2O, and reemitted back towards Earth's surface heating air temperature near Earth's surface [1]. This phenomenon is called the greenhouse effect and it helps to maintain a comfortable temperature for Earth's habitants as without greenhouse gases Earth's surface temperature would be much colder [2]. Since the Industrial Revolution greenhouse gas content in the atmosphere has increased significantly, in particular, CO_2 accounting for a 50% rise [3]. It increased the average Earth's temperature to 1.0 °C compared to pre-industrial revolution time, otherwise known as global warming [4]. Global warming affects negatively all forms of life on the Earth and the economies [5].

The governments of 195 countries agreed to make combined efforts to mitigate climate change in Paris in 2015. Paris Agreement set the goal to limit a global temperature rise in the 21st century well below 2 degrees Celsius above pre-industrial levels [6]. In order to achieve this goal, greenhouse emissions should be reduced by 45% by 2030 and reach net zero by 2050 [7]. The global shift towards renewable technologies is motivated by these climate targets.

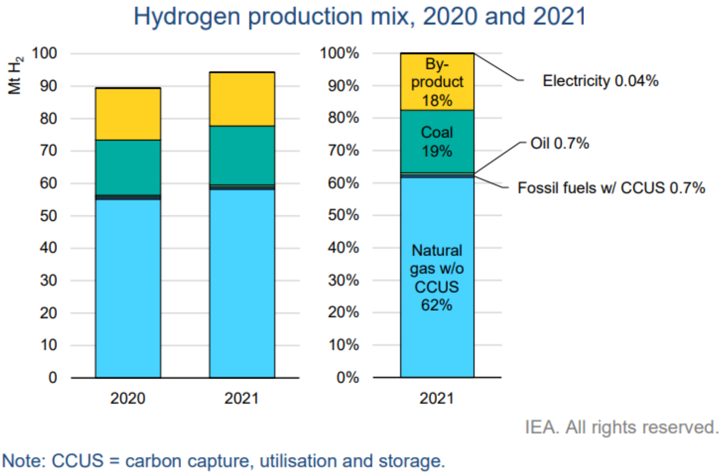
Hydrogen production mix, 2020 and 2021

IEA. All rights reserved.

Note: CCUS = carbon capture, utilisation and storage.

Figure 1.1: Global hydrogen production in 2020 and 2021 [8]

According to the Global Hydrogen Review 2022 [8] report prepared by the International Energy Agency global hydrogen production reached 94 million tonnes in 2021 with corresponding 900 million tonnes of CO_2 emissions. Almost 200 million tonnes of hydrogen should be produced by 2030 to be on track for net zero emissions by 2050. Only 35 kilotonnes out of 94 million tonnes of hydrogen were produced via water electrolysis. An enormous effort is needed to bridge the gap in total hydrogen production and make the production process environmentally friendly.

1.2. Decarbonization

The hydrogen is classified as grey, blue and green depending on CO_2 emissions involved during hydrogen production. The hydrogen produced by steam methane reforming (SMR) or coal gasification is called grey hydrogen. SMR plant emits 7 kg CO_2/ kg H_2 on average, while coal gasification results in 19-23 kg CO_2/ kg H_2 [9, 10]. The grey hydrogen production incorporated with carbon capture and storage is referred to as blue hydrogen. Blue hydrogen can not be a long-term solution since not all CO_2 can be captured and additional CO_2 is emitted during the production process making blue hydrogen's CO2 footprint only 9-12 % less compared to grey hydrogen [11]. The hydrogen produced from electrolysis using renewable energy sources is called green hydrogen. Green hydrogen is environmentally more sustainable compared to blue and grey hydrogens, however, only 4 % of global hydrogen production is based on water electrolysis [12]. Green hydrogen has great potential to significantly reduce CO_2 emissions in various industries.

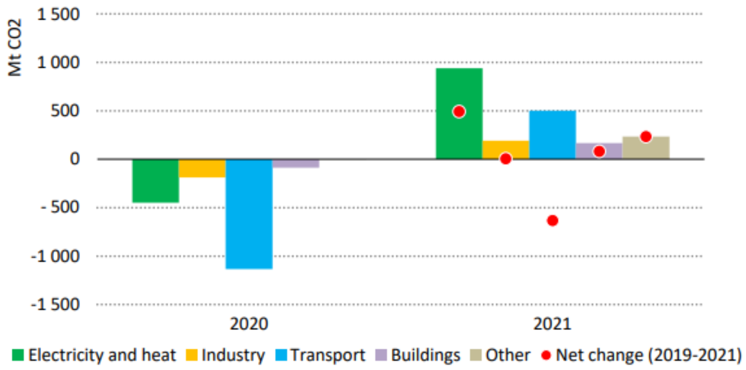

Figure 1.2: Global CO_2 emissions in 2020 and 2021 [13]

Currently, major hydrogen application attributes to ammonia production. In the Haber-Bosch process, hydrogen is reacted with nitrogen to produce ammonia. Hydrogen used in the reaction comes from steam methane reforming (SMR) and water gas shift (WGS) reactions. The issue with conventional technology is CO_2 emission. Replacing hydrogen produced from SMR and WGS with green hydrogen can help solve the problem.

The steel industry is responsible for 7-9 % of global CO_2 emissions generating an average of 1.85 tonnes of CO2 per tonne of crude steel [14]. The integration of hydrogen in the steel industry could reduce CO2 emissions by 90 % [15].

The buildings and heating sector make up one-third of all energy demand and is responsible for 12% overall emissions [12]. The main feedstocks for heat generation are fossil fuels such as coal, oil and natural gas. The emitted CO_2 varies depending on the fossil fuel type. It is beneficial to combust green hydrogen instead of fossil fuel as hydrogen combustion product does not have any CO_2.

Transportation accounts for approximately 22 % of overall CO2 emissions [12]. The current use of hydrogen is attributed to fuel-cell electric vehicles (FCEV). The number of FCEVs has been growing steadily and reached the value of 59000 by end-June 2022 [8]. Expected hydrogen application expansion to heavy-duty vehicles and maritime in the near future suggests an increase in demand for hydrogen.

1.3. XINTC B.V.

XINTC is a Dutch start-up company established in 2012. XINTC develops, produces and markets smart alkaline electrolysis with a capacity range between 150 kW and 50 MW. The use of abundant materials in electrolyser manufacturing and a modular design approach gives XiNTC advantages in flexible production scale and levelised cost of hydrogen over its competitors. XINTC electrolysers come as containerized units. The produced hydrogen can be delivered to the end user with a pressure of up to 30 bar.

Figure 1.3: Modular design concept

1.4. Research questions

Hydrogen produced from water electrolysis contains impurities such as oxygen and water vapour. Hydrogen contamination occurs due to oxygen crossover [16]. The ability of hydrogen to hold water vapour is governed by vapour-liquid equilibrium and increases with lower pressures [17].

Predominantly pure hydrogen is used in ammonia production, refining and transportation [18]. The purity level of pure hydrogen varies from 99.99 % and 99.999 % depending on the application [19].

The hydrogen for fuel cell vehicles is compressed up to 875 bar in order to store it efficiently in a given volume. The hydrogen expansion during the refuelling process involves a non-negligible temperature rise due to the negative Joule-Thompson coefficient at this pressure level. During the filing process, the temperature should be kept below 85°C to avoid mechanical disintegration of the tank and for that reason, the compressed hydrogen needs to be brought to temperatures between -33°C and -40°C before refuelling. The presence of water in hydrogen might lead to ice formation during the cooling process, which can restrict hydrogen flow in the system [20].

Oxygen impurity constraints come from ISO 14687:2019 [21] which describes impurity requirements for hydrogen applied in proton exchange (PEM) fuel cells. The carbon-supported platinum and platinum alloy catalyst employed as an anode in the PEM fuel cell is susceptible to liquid water which is formed by hydrogen and oxygen reaction [22, 23]. The possible reason for limiting oxygen impurity is linked with catalyst protection.

Oxygen and water vapour content in hydrogen should be constrained to very low levels due to the above-mentioned reasons. Thus, it is necessary to post-process hydrogen produced from water electrolysis. The post-processing steps include storage, cooling, catalytic purification and drying of hydrogen using PSA or TSA.

The ultimate task is to design the hydrogen-purifying process with a production rate of 400 kg of pure hydrogen per day which is equivalent to 1 MW electrolyser capacity. And the design should be efficient in terms of energy and cost. Therefore, the following research questions have been formulated:

- How to model the deoxygenation and drying units to obtain process design objectives?
- How does adsorbent material affect adsorption and bed regeneration?
- How to maintain continuous adsorption and desorption operations?
- How to minimize the energy input required to purify hydrogen?

2

Literature study

2.1. Hydrogen production

The researches mainly focus on keeping hydrogen concentrations below the explosive limit 4% on the oxygen side of an electrolyser as the hydrogen crossover is higher than the oxygen crossover [24]. It means hydrogen contamination with oxygen is below 4% and impurity concentrations in hydrogen depend on the type of water electrolysis technology [25]. Therefore a brief summary of common water electrolysis technologies will be given below.

2.1.1. Alkaline water electrolyser

Alkaline water electrolysis cells consist of an anode and cathode submerged in a liquid electrolyte. The base KOH or NaOH is used to prepare an electrolyte as the conductivity of pure water is very low. KOH or NaOH concentration in electrolyte vary from 25 wt% to 40 wt%. Oxygen evolution and hydrogen evolution reactions take place at the anode and cathode respectively.

$$\text{Cathode (HER)} : 2\text{H}_2\text{O} + 2\text{e}^- \rightarrow \text{H}_2 + 2\text{OH}^- \tag{2.1}$$

$$\text{Anode (OER)} : 2\text{OH}^- \rightarrow \frac{1}{2}\text{O}_2 + \text{H}_2\text{O} + 2\text{e}^- \tag{2.2}$$

The anode and cathode are separated by a diaphragm to prevent gas mixing. The diaphragm material should have high ionic conductivity to reduce Ohmic losses and should be able to withstand operating temperature, which is between 70°C and 90°C for AWE. The advantage of AWE is that it is a well-known technology and cheaper compared to other electrolysers because does not require noble metal catalyst material. The disadvantages are related to hydrogen contamination by oxygen due to gas crossover and limited operating current density range (0.2-0.8 A cm^{-2}).

2.1.2. Proton exchange membrane electrolyser

The key component of the PEM electrolyser is a polymeric membrane coated with a catalyst. Nobel metals such as platinum and iridium are used as a catalyst to resist the acidic environment of the membrane (pH$\sim$2) [26]. The electrodes can be placed very close to the membrane enabling a compact design. The half-reactions on the anode and cathode are as follows:

$$\text{Cathode (HER)} : 2\text{H}^+ + 2\text{e}^- \rightarrow \text{H}_2 \tag{2.3}$$

$$\text{Anode (OER)} : \text{H}_2\text{O} \rightarrow \frac{1}{2}\text{O}_2 + 2\text{e}^- + 2\text{H}^+ \tag{2.4}$$

The operating temperature of PEM electrolyser is within the range of 50°C and 80°C. PEM electrolyser provides pure hydrogen and can operate at a higher current density range (1-3 A cm^{-2}) compared to AWE electrolysers. It is also possible to increase the pressure on the cathode side, which allows the end user to save energy on hydrogen compression. The high cost of PEM associated with catalyst material makes it less competitive in the market.

2.1.3. Anion exchange membrane electrolyser

Anion exchange membrane electrolysers feature the advantages of PEM and AWE electrolysers. The solid electrolyte coupled with anion exchanging membrane allows for obtaining high-purity hydrogen. Similar to AWE electrolysers, hydroxide ions are employed for charge transfer in AEM electrolysers. The electrochemical reactions taking place on anode and cathode are described below:

$$\text{Cathode (HER)} : 4\text{H}_2\text{O} + 4\text{e}^- \rightarrow 2\text{H}_2 + 4\text{OH}^- \tag{2.5}$$

$$\text{Anode (OER)} : 4\text{OH}^- \rightarrow \text{O}_2 + 2\text{H}_2\text{O} + 4\text{e}^- \tag{2.6}$$

The reported operating current density range is between 0.2 and 2 A cm^{-2}[27]. AEM electrolysers have stability issues and the possibility of scaling technology up is not certain despite its advantages in the current density range and cost.

2.2. Purificaion methods

The present gas purification technologies include adsorption, membrane separation (metal and polymer membranes), metal hydride separation, cryogenic distillation and catalytic purification. The driving force for membrane separation is the pressure difference. The scale of use is a restricting factor of membrane separation. In cryogenic distillation, the separation is performed using differences in the volatility of components. The cryogenic distillation application is limited due to high energy consumption. Metal hydride separation is based on the ability of metals to absorb and desorb gases. Problems in metal hydride separation are associated with material stability and a slow rate of release [28]. Catalytic purification and adsorption have been chosen as optimal separation methods taking into account scale of use, material constraints, energy consumption and feed composition.

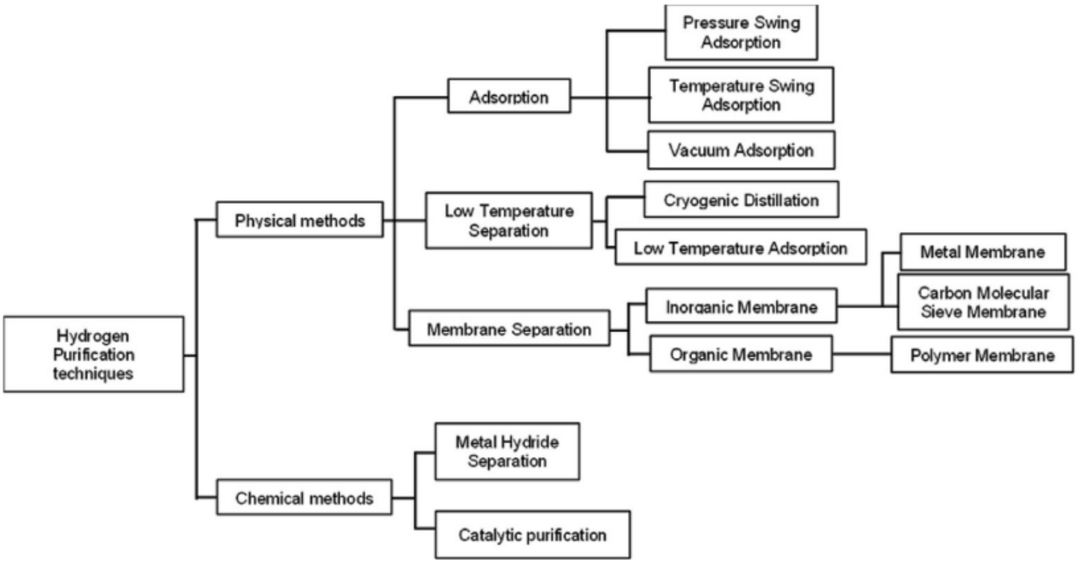

Figure 2.1: Purfification methods calssfication [29]

2.2.1. Deoxygenation

The O_2 content in H_2 stream is typically in the range of 0.2-0.6% depending on the electrolyser type, which is above the threshold, 5 ppm [30]. Catalytic recombination of oxygen and hydrogen theoretically can decrease oxygen levels to zero without an external energy supply if an appropriate catalyst is selected.

Predominantly Pt and Pd are used as the catalyst material for the recombination of oxygen and hydrogen. The metals can absorb hydrogen and undergo structural deformation because of it. Therefore, various Pt and Pd combinations with TiO_2, Al_2O_3 and SiO_2 are applied to solve the problem of catalyst material stability. Catalysts are prone to deactivation due to thermal degradation and water poisoning.

Yorik et al. [30] used 1.2%Pd/Al_2O_3 catalyst to remove oxygen from a wet hydrogen stream with 0.2% water content. Feed enters to deoxygenation unit at room temperature, but heats up to 50-55°C because of the exothermic nature of the reaction. Oxygen content maintained below 4ppm. Issues with catalyst embrittlement and deactivation are not mentioned after 500 minutes experiment duration.

Sang Ge et al. [31] investigated hydrogen and oxygen recombination reaction assisted with 0.2% Pt/Al_2O_3 catalyst. The hydrogen and oxygen recombination reaction with a molar ratio of 2:1 in feed resulted in the high-temperature range between 100°C and 600°C. Feed rate, cooling and hydrogen feed distribution systems are used to control temperature and achieve uniform temperature distribution in a reactor. Reported hydrogen conversion is close to 100%. The catalyst deactivation has been observed when the reaction temperature was above 900°C.

Lalik et al. [32] compare Pd, Pt and a combination of Pd-Pt catalysts, supported by Al_2O_3 and SiO_2, tendency to deactivate due to water formation coming from hydrogen and oxygen recombination reaction. Pd/SiO_2 shows higher H2 conversion rate compared to Pt/SiO_2 and Pt/Al_2O_3 in stream with composition 0.5 vol% H2 and 3 mol% H2O at 25°C. Hydrogen conversion improves when the temperature is increased to 50°C. Lalik et al point out that catalysts with Pt are more vulnerable to water poisoning compared to catalysts with Pd.

Most studies focus on removing hydrogen from waste streams in nuclear plants. Only Yorik et al. [30] describes catalytic purification application to remove oxygen from hydrogen stream.

2.2.2. Hydrogen drying

Adsorption is a well-established technology which has become the common choice for gas purification and drying. Adsorption exploits the phenomenon of substances accumulating on solid surfaces when exposed to it. Depending on the nature of the bond created between gas and solid phases two types of adsorption, namely physisorption and chemisorption, are classified. In physisorption interactions between molecules are mainly governed by van der Waals forces. Whereas in chemisorption a strong bond between molecules is formed. However, a reliable method of distinguishing physisorption from chemisorption does not exist in practice [33].

The key element of efficient adsorption system design is a proper interpretation of adsorption isotherms. Adsorption isotherm describes the dynamic equilibrium between molecules in the fluid phase and solid phase. The adsorption isotherm is represented by the amount of adsorbate per unit mass of adsorbent as a function of pressure at a constant temperature. Normally adsorption isotherms are obtained from experiments. Therefore, Refs. [34, 35, 36, 37] have been studied to understand water loading on zeolites, activated alumina and silica gel. In order to have an accurate comparison, adsorption isotherms at the same temperature have been selected.

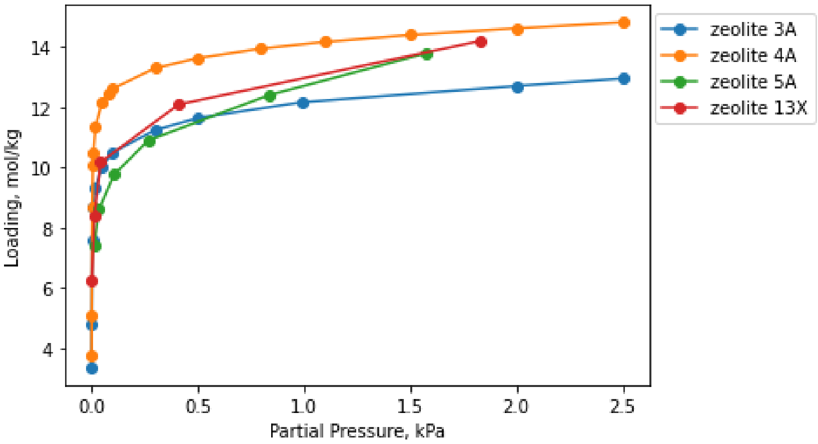

Figure 2.2: Pure water adsorption on zeolites at 25°C [35, 36]

As it can be seen in Figure 2.2 water adsorption isotherm on zeolites have a similar shape and the highest water loading capacity can be achieved by zeolite 4A. Only by analysing the shape of the adsorption isotherm, a few design remarks can already be made. For example, water loading does not increase sufficiently above a partial pressure of 1 kPa, which means compressing feed above a certain total pressure is not needed. Also, it can be observed that zeolites have high water uptake even at low partial pressures. It makes zeolites suitable for purifying gases with low water concentration in the feed.

Figure 2.3 shows pure water adsorption on silica gel and activated alumina and compares it with zeolite with the best water loading performance. It can be seen that above partial pressure of 1.5 kPa, silica gel and activated alumina have higher water loading compared to zeolite. In this case, the choice of adsorbent might depend on feed composition because it determines partial pressure. The desorption curve for activated alumina was included in the plot to highlight the difference between adsorption and desorption.

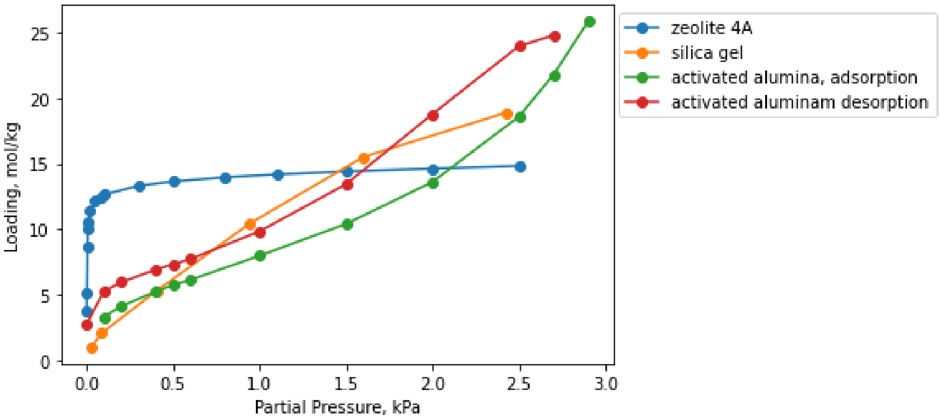

Figure 2.3: Pure water adsorption on activated alumina and silica gel at 25°C [34, 37]

The adsorption isotherms of only pure water on different adsorbents have been considered until now. But since the objective is to separate gas mixture, the area of interest is selectivity. Selectivity describes the tendency of one component of the mixture to get adsorbed more strongly compared to other components. Scientific research focused on identifying adsorption isotherms for hydrogen and water vapour mixture has not been found. The pure hydrogen adsorption on silica gel and zeolite 5A is obtained from Refs. [38] and [39]. Based on acquired data hydrogen can be considered an inert gas in general as hydrogen loading compared to water is very low.

Adsorption isotherm for pure component and adsorption isotherm for the same component in a mixture differ. Wang et al. [36] compares the adsorption of pure CO2 and CO2 in the presence of water vapour on zeolite 13X. The performed experiments demonstrate a decrease in CO2 uptake with an increase in water content in the stream. He also mentions the ideal adsorbed solution theory (IAST) and viral excess mixing coefficient (VEMC) models used for adsorption isotherm generation for multicomponent gases. The theory behind IAST and derivations is explained in detail in Ref. [40].

To separate gas, feed consisting of a gas mixture is put through a column filled with porous solid adsorbent. The mixture component with stronger attraction to a solid surface is retained in the adsorption column and the product with the required purity is obtained at the column outlet. Adsorbent regeneration is needed for cost-effective operation. The key parameters for the regeneration of the adsorption column are pressure and temperature. Depending on the chosen regeneration method adsorption separation systems are mainly divided into pressure swing adsorption (PSA) and temperature swing adsorption (TSA).

PSA utilizes the loading dependency on partial pressure. The compressed feed is supplied to the column to initiate the adsorption process. In contrast, desorption favours low pressures. The partial pressure is lowered by blowing down the column and purging by inert gas or product. Conventional PSA is not always able to regenerate the adsorption bed. As can be seen from Figure 2.3, zeolites require very low partial pressure for regeneration. In this case, regeneration is conducted under vacuum conditions and the method is called VPSA. PSA is commonly used in hydrogen purification, noble gases

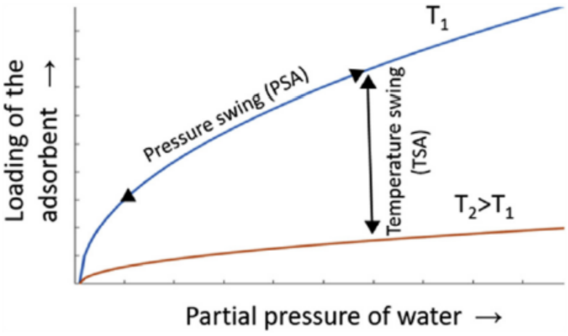

Figure 2.4: Regeneration method. The fixed be can be regenerated by reducing pressure or increasing the temperature. Depending on chosen regeneration method adsorption separation systems are mainly divided into pressure swing adsorption (PSA) and temperature swing adsorption (TSA) [30]

purification and air separation.

In TSA adsorption is performed at lower temperatures and adsorption bed regeneration is achieved by supplying heat. The heated regeneration gas is fed to the adsorption column to elevate the bed temperature. After the desorption step, cold regeneration gas is supplied to prepare a bed for the adsorption step. TSA leverages adsorbent capacity as full adsorbent regeneration can be obtained by increasing the temperature. Refs. [41, 42, 43] suggest that TSA application is considered when the adsorbent material has a strong affinity to adsorb molecules such as zeolite. Typically TSA is used in natural gas dehydration and CO_2 capture.

The comparison of PSA, TSA and VSA applications for the purification of hydrogen produced from SMR is given by Ayub et al [42]. The adsorption consisting of activated carbon and zeolite 5A layers is used to purify hydrogen to fuel cell standards (H_2 purity > 99.99, CO impurity < 0.2 ppm). The feed mainly consists of 75% H_2 and the rest is impurities: 18%CO_2, 3.2%H_2, 0.7% CO and 3.2% N2. The column is pressurized with product in PSA 1, whereas the feed is used for the same purpose in PSA 2. PSA1, VSA and TSA were able to meet purity requirements. PSA 1 is less attractive because of low hydrogen productivity compared to TSA and VSA. The energy consumption of VSA and TSA are 0.94 MJ/kgH_2 and 45.62 MJ/kgH_2 respectively. VSA is recommended as the optimal hydrogen purification technology taking into account productivity and economics. The conclusions drawn by Ayub et al might not be relevant to the purification of hydrogen produced from water electrolysis, because it has only O_2 and H_2O impurities in low concentrations.

The adsorption system performance assessment is based on product purity, recovery and adsorbent productivity. Product purity is defined as the amount of pure substance in a product divided by the total product amount. Product recovery is defined as the amount of component in a product stream divided by the amount of the same component in the feed stream. Adsorbent productivity is measured by the amount of product or feed mixture processed per unit amount of adsorbent per unit time [44].

The adsorption system has at least two columns where adsorption and desorption take place simultaneously to maintain continuous operation. The complete cycle includes pressurization, adsorption, counter-current blow down and purge steps according to Skarstorm. The first column is pressurized with feed, then followed by the adsorption step. Meanwhile, the second column is blown down and purged to regenerate. The hydrogen post-processing scheme proposed by XINTC implies purging the adsorption column using the product, which is recycled by sending it back to the feed. This approach helps to prevent product loss. The scheduling steps become more complex with the increasing number of columns.

Purification is performed with help of a multilayered adsorbent bed in case of multicomponent gas mixture [45]. Because a single adsorbent can not efficiently separate all gases. Since oxygen is planned to be removed by catalytic recombination of oxygen and hydrogen, a multilayered bed is not needed for binary mixture purification.

Loading, selectivity, kinetic and transport properties, regeneration method, cost, chemical and thermal stability should be considered in adsorption selection [46]. Silica gel, activated alumina and zeolites

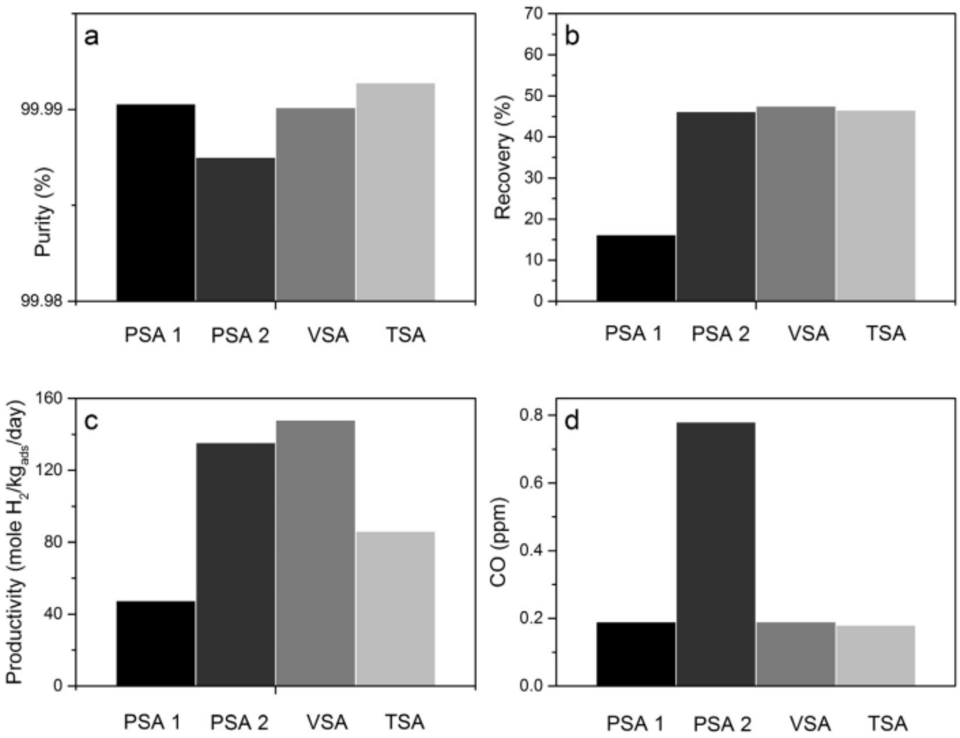

Figure 2.5: The comparison of regeneration methods [42]. In PSA 1, the adsorption column is pressurized with the product, whereas in PSA 2, the adsorption column is pressurized with the feed.

are commonly used for the removal of water vapour from gases [47]. As mentioned earlier zeolites provide high water loading even at low concentrations, but it is the most expensive adsorbent compared to others. Also, zeolite regeneration might consume more energy. Silica gel has the highest water loading but tends to shutter in the presence of liquid water [47]. Activated alumina is the least expensive adsorbent with high water loading. Activated alumina can also tolerate the presence of alkaline impurities. Information on adsorbent performance degradation over operation time has not been found. The important adsorbent properties are listed in the table below:

Table 2.1: Adsorbent properties. Data obtained from Ref. [48]

Adsorbent	**Pore diameter** d_p, A°	**Particle porosity** ϵ_p	**Particle density** ρ_p, g/cm^3	**Surface area** S_g, m^2/g
Activated alumina	10-75	0.50	1.25	320
Silica gel:				
small pore	22-26	0.47	1.09	750-850
large pore	100-150	0.71	0.62	300-350
Zeolites	3-10	0.2-0.5	1.4	600-700

2.3. Purification methods integration

Zhemin Du et al. [49] review each purification method and comes to the conclusion that none of the methods is able to purify hydrogen to ISO 14687: 2019 standard standalone. Then the possible solution can be found by integrating purification methods.

The recent experimental study on the purification of hydrogen produced from 50kW alkaline electrolyser was conducted by Yorick et al. [30]. Hydrogen post-processing steps include removing an electrolyte and reducing oxygen and water content until required by ISO 14687:2019 standard. First, wet hydrogen is fed to the scrubber, where it goes through deionized water to remove KOH. In the following step, recombination of hydrogen and oxygen assisted with catalytic bed takes place in dexor. The final step, water removal is done using PSA with vacuum regeneration. Before PSA, the stream is cooled down and compressed to 40 bar as adsorption favours high pressure and low temperature.

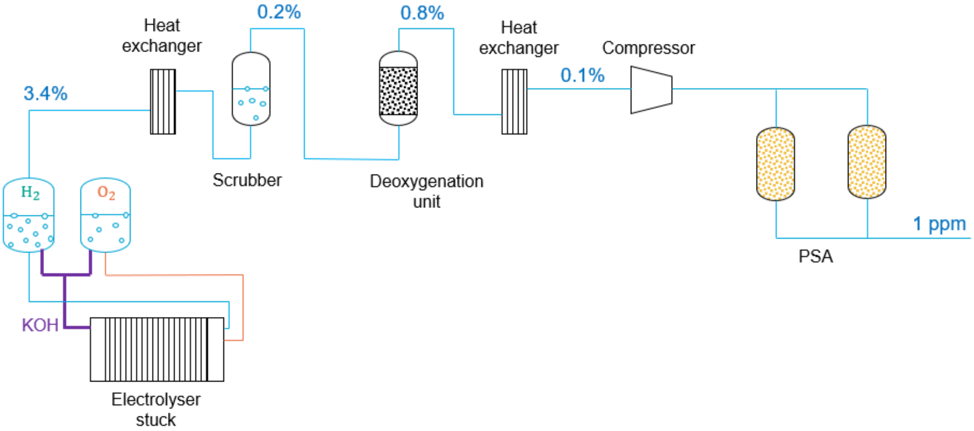

Figure 2.6: Process flow diagram [30]. The percentages displayed in the flow diagram represent the water content in the stream after each purification process step

The reported product recovery is 98.4% and the energy consumption is 0.5 kWh/kg H2. Pressure equalization in the blowdown step and reduction of purge rate due to vacuum pump use helped to increase product recovery. After all hydrogen post-processing steps, the water content was reduced from 3.4% to 1 ppm, whereas the oxygen content in the product varied between 1 ppm and 4 ppm.

The water electrolysis is performed at atmospheric conditions as safety requirements for materials are lower at atmospheric conditions. As a result, the production cost can be reduced. On the other hand, pure hydrogen should be stored at higher pressures to increase the amount of hydrogen in the given volume. The proposed hydrogen post-processing plant design intends to satisfy both demands.

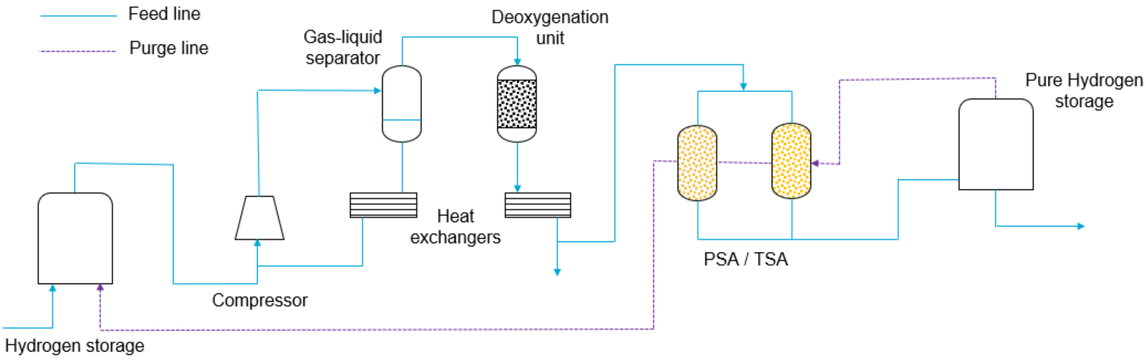

Figure 2.7: Process flow diagram by XINTC B.V. The

The main design components are a liquid ring compressor, deoxygenation unit and adsorption column. Deoxygenation and adsorption were discussed in the previous section. The liquid ring compressor uses rotating liquid for suction and compression of gas. Typically, a single-stage liquid ring compressor produces nominal pressure in the range of 1.5 bar and 2.2 bar. The liquid ring compressor is comprised of an impeller enclosed in a casing filled with operating liquid. The liquid ring is created when the impeller reaches a certain rotation speed because of centrifugal force. Periodically changing volume in crescent-shaped cavities creates suction and compression. One of the advantages of the liquid ring compressor compared to other compressors is isothermal compression, which makes it suitable for flammable and explosive gas compression. The liquid ring compressor is applied in argon production and hydrogen transportation [50].

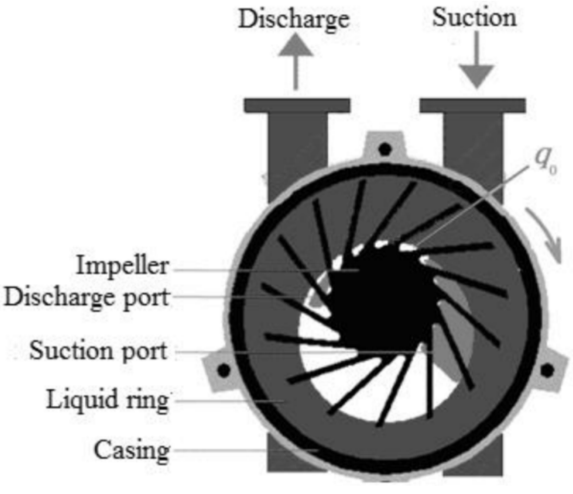

Figure 2.8: Liquid ring compressor[50]

The produced hydrogen with impurities is stored in the tank before being sent to the liquid ring compressor. The part of the water is knocked out during the compression process because water solubility in hydrogen reduces with temperature increase [17]. After the compression step, the stream goes to the deoxygenation unit where catalytic recombination of hydrogen and oxygen takes place. The reaction generates heat and produces additional water, which is not preferred for adsorption. Therefore, the heat exchanger is placed after the deoxygenation unit to cool down the flow and remove condensed water. The final step of purification is water removal using adsorption. Primary features of the design in contrast to Yorick et al work are a scale of hydrogen production, feed composition, removing part of the water from the system before the adsorption column and recycling of purge. There are concerns regarding the location of the deoxygenation unit in the hydrogen post-processing scheme. The catalyst material exposed to high pressures (up to 30 bar) might have a stability issue. Moreover, water solubility in hydrogen is low at high pressures, which means more liquid water is present and that causes catalyst deactivation. Placing deoxygenation before the compressor can solve these issues, but then heated gas needs to be compressed due to an exothermic reaction. Compressing heated gas is not an option, therefore the cooling system should be introduced before the compressor. The cooling will cost energy. The configuration optimization mentioned in the research questions section is intended to address this problem.

2.4. Design concepts

The gas separation in fixed bed adsorption is obtained by putting mixture flow via a column packed with adsorbents. A mixture component with strong affinity is trapped in the adsorption column and pure gas comes out of the column. The adsorption column can not retain all impurities once the adsorption capacity is utilized fully. As result, the purity of the adsorption column downstream will be affected. Therefore, it is important to predict a breakthrough time to switch columns and maintain the purity of the product. Hence, the mass balance should be solved to calculate the concentration as a function of time and bed length. The 1D mass balance equation is employed to avoid the complexity of 2D, which comes with a high computational cost:

$$\frac{\partial c_i}{\partial t} + \frac{\partial (c_i u_i)}{\partial z} - D\frac{\partial^2 c_i}{\partial z^2} = -\left(\frac{1-\epsilon_b}{\epsilon_b}\right)\frac{\partial q_i}{\partial t} \tag{2.7}$$

In reality, the concentration front inside the column does not move uniformly and breakthrough happens before full adsorption capacity utilization. This phenomenon is captured in the mass balance equation by including the axial dispersion coefficient, D.

The breakthrough curve shown in figure 2.9 plays an important role in identifying the adsorption bed length (L_b) and the length of the unused bed (LUB). The adsorption takes place in the region between

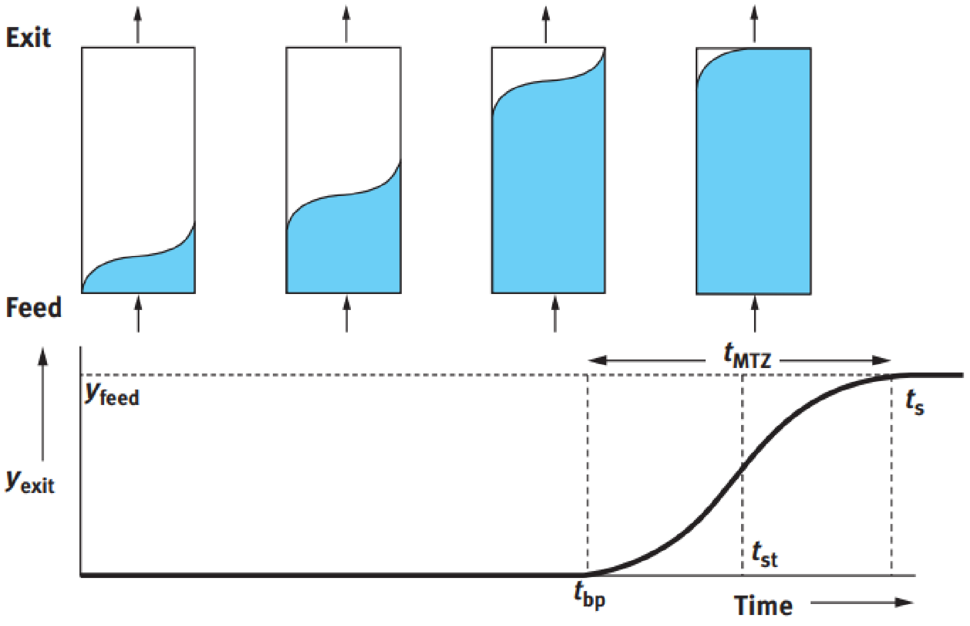

Figure 2.9: Breakthrough curve [51]

t_{bp} and t_s, which is called the mass transfer zone (MTZ). Reducing mass transfer resistance results in a more flat breakthrough curve and subsequently decreases LUB. Keller et al. [52] suggest the following equation to calculate bed length:

$$\text{LUB} = \left(1 - \frac{t_{bp}}{t_{sat}}\right) \mathsf{L}_b \tag{2.8}$$

The adsorption generates heat because of its exothermic nature. On the other hand, the adsorption rate decreases with temperature increase. Therefore, the temperature inside the column needs to be controlled. Most heat generation takes place in the mass transfer zone. Temperature profiles can be determined from the energy balance equation [53]:

$$\frac{\partial T_f}{\partial t} + \left(\frac{1-\epsilon_b}{\epsilon_b}\right) \frac{\rho_s c_{p,s}}{\rho_s c_{p,f}} \frac{\partial T_s}{\partial t} = \frac{k_f}{\rho_f c_{p,f}} \frac{\partial^2 T_f}{\partial z^2} - u_f \frac{\partial T_f}{\partial z} - \frac{4h}{\epsilon_b d \rho_f c_{p,f}} (T_f - T_w) + \left(\frac{1-\epsilon_b}{\epsilon_b}\right) \frac{\partial q_i}{\partial t} \frac{-\Delta H \rho_s}{\rho_f c_{p,f}} \tag{2.9}$$

The one of strategies to prevent temperature increase in the adsorption column might be using several small columns in parallel instead of a single column with a large diameter [54].

Total pressure decrease leads to a decline in the adsorption rate. Pressure drop in the adsorption column should be minimized to adsorption rate disruption. Pressure drop is calculated using Ergun's equation:

$$\frac{\Delta p}{L_b} = \left(\frac{f_t C_t G^2}{\rho_f D_{pe}}\right) \tag{2.10}$$

The fixed bed adsorption design approach includes the following steps:

1. Select the adsorbent material based on required product purity, feed gas composition and cost
2. Determine the allowable gas superficial velocity based on a specified pressure drop limitation
3. Calculate the required bed cross-section area and/or the number of beds of a given diameter based on the superficial velocity selected in step 2
4. Select cycle time and calculate the quantity of adsorbent required based on an estimated end-of-life equilibrium capacity

5. Determine total bed height based on the volume of the adsorbent calculated in step 4 and an estimated length of the mass transfer zone
6. Calculate the total heat required during the regeneration step to heat and desorb the adsorbate, heat the adsorbent, heat the vessel and internals, heat the exit gas, and provide for heat losses through the vessel walls
7. Establish a heating/cooling time schedule based on the cycle time selected in step 4, and calculate the regeneration gas flow rate required to provide the needed in the time available

The last two steps are specific to TSA.

Modelling an adsorption system involves solving a set of nonlinear partial differential equations coming from mass, energy and momentum balances in the space and time domain. The appropriate numerical solver will be selected and described in detail in the modelling section of the thesis project.

3
Model Description

As a compromise between the computational power required and the level of accuracy, the adsorption process is modelled using a one-dimensional axially dispersed plug flow approach. The model combines all mechanical dispersion effects into the axial dispersion term. The assumption is made that the flow behaves as a plug, meaning there are no variations in velocity, concentration, temperature, or porosity in the radial direction. The gas phase described by ideal gas law. The adsorbent properties and bed porosity are assumed to be uniform across the column.

3.1. Process variables

Pressurization, adsorption, desorption, and depressurization are the four basic PSA/TSA cycle steps. For a system to be designed that can purify hydrogen to the ISO 14687: 2019 standards [21], it is crucial to grasp the variations in concentration, pressure, temperature, and loading during each step. Mass, energy, and momentum balances need to be solved to obtain these process variables.

3.1.1. Mass balance

The concentration is derived from mass balance (see Appendix A.1):

$$\frac{\partial c_i}{\partial t} + \frac{\partial (c_i u)}{\partial z} - D_L \frac{\partial^2 c_i}{\partial z^2} = -\frac{(1-\varepsilon)}{\varepsilon} \sum_{i=1}^{N_c} \frac{\partial q_i}{\partial t} \rho_s \tag{3.1}$$

where c_i is a concentration of component i , D_L is the axial diffusion coefficient, u is interstitial velocity, ε is bed porosity and $\partial q_i/\partial t$ is loading change.

3.1.2. Energy balance

Adsorption favours lower temperatures because the loading on the adsorbent material is higher at lower temperatures, as depicted in Figure 3.1. However, it is important to note that adsorption is an exothermic process that releases heat. As shown in Figure 2.4, in addition to controlling pressure, regulating the temperature is also crucial in influencing the adsorption process. Temperature changes in time and space can be obtained by solving the energy balance equation. The energy balance equation is described in scientific papers [56] in both simplified and extended versions.

Simplified energy balance

Heat is generated within solid adsorbent particles during adsorption, and immediate thermal equilibrium between solid adsorbent particles and gas is assumed in simplified energy balance. Energy

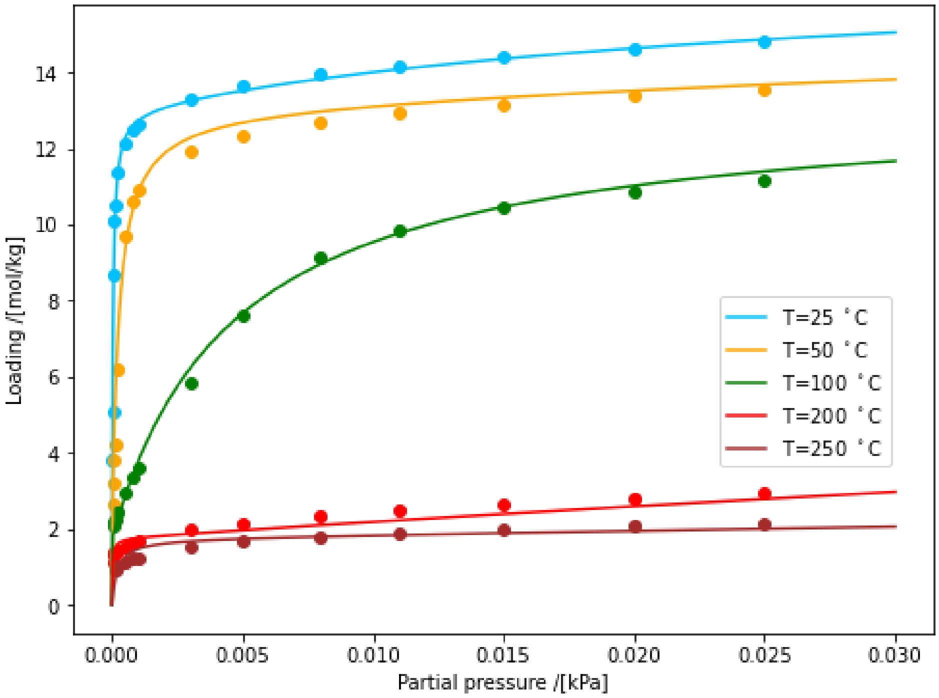

Figure 3.1: Temperature-dependent water adsorption on Zeolite 4A. Experimental data are represented by dots, and the lines are generated using the triple-site Langmuir model fitted to the experimental data. Experimental data and fit parameters are based on Ref.[55]. Fit parameters can be found in Table 3.2

balance for gas phase (see Appendix A.2):

$$\left(C_{p,f}\rho_f + \frac{1-\varepsilon}{\varepsilon}C_{p,s}\rho_s\right)\frac{\partial T_f}{\partial t} = k_{eff}\frac{\partial^2 T_f}{\partial z^2} - C_{p,f}\rho_f u\frac{\partial T_f}{\partial z} - \frac{4h_w}{\varepsilon d_i}(T_f - T_w) - \sum_{i=1}^{N_c}\rho_s\left(\frac{1-\varepsilon}{\varepsilon}\right)\frac{\partial q_i}{\partial t}\Delta H_i \tag{3.2}$$

The heat of adsorption is dissipated to the environment through the column wall. Therefore the wall temperature is involved in the gas energy balance. The wall temperature is based on wall energy balance (see Appendix):

$$\rho_w C_{p,w}\frac{\partial T_w}{\partial t} = k_w\frac{\partial^2 T_w}{\partial z^2} + \frac{4d_i}{(d_i+t_w)^2 - d_i^2}h_w(T_f - T_w) - \frac{4(d_i+t_w)}{(d_i+t_w)^2 - d_i^2}h_\infty(T_w - T_e) \tag{3.3}$$

The assumption made is that the wall temperature varies solely in the axial direction.

Extended energy balance

In an extended energy balance, thermal equilibrium is not assumed between the gas and solid adsorbent particles. Therefore, separate energy balances are considered for the gas phase, solid adsorbent, and wall (See Appendices A.3, A.4, A.5). Energy balance for gas phase:

$$\rho_f C_{p,f}\frac{\partial T_f}{\partial t} = k_f\frac{\partial^2 T_g}{\partial z^2} - \rho_g u C_{p,f}\frac{\partial T_f}{\partial z} - \frac{4}{\varepsilon d_{\text{in}}}h_w(T_f - T_w) + \left(\frac{1-\varepsilon}{\varepsilon}\right)\frac{1}{\Delta z}h_f(T_s - T_f) \tag{3.4}$$

Energy balance for solid phase:

$$\rho_s C_{p,s}\frac{\partial T_s}{\partial t} = k_s\frac{\partial^2 T_s}{\partial z^2} - \frac{1}{\Delta z}h_f(T_s - T_f) + \sum_{i=1}^{N_c}\rho_s\frac{\partial q_i}{\partial t}\Delta H_i \tag{3.5}$$

Energy balance for a wall:

$$\rho_w C_{p,w}\frac{\partial T_w}{\partial t} = k_w\frac{\partial^2 T_w}{\partial z^2} + \frac{4d_{\text{in}}}{(d_{\text{in}}+t_w)^2 - d_{\text{in}}^2}h_w(T_f - T_w) - \frac{4(d_{\text{in}}+t_w)}{(d_{\text{in}}+t_w)^2 - d_{\text{in}}^2}h_\infty(T_w - T_e) \tag{3.6}$$

The terms used in the above equations are given below:

- c$_i$ is the concentration of component i (mol/m^3)
- D$_L$ is the axial dispersion coefficient (m^2/s)
- q$_i$ is the loading of component i (mol/kg)
- T$_g$ is the gas temperature (K)
- T$_s$ is the solid adsorbent particles temperature (K)
- T$_w$ is the temperature of column wall (K)
- T_e is the environment temperature (K)
- C_{ps} and C_{pg} are the specific heat capacities of the solid and gas phases, respectively (J/kgK)
- ρ_g is the gas density (kg/m^3)
- ρ_s is the solid adsorbent particle density (kg/m^3)
- ρ_w is the wall density(kg/m^3)
- k_{eff} is the effective thermal conductivity of the bed (W/mK)
- k_g is the thermal conductivity of the gas (W/mK)
- k_s is the thermal conductivity of the solid adsorbent particles (W/mK)
- k_w is the thermal conductivity of the column wall material (W/mK)
- ΔH is the heat of adsorption (J/mol)
- C_{pg} is the specific heat capacity of the gas (J/kgK)
- C_{ps} is the specific heat capacity of the solid adsorbent particles (J/kgK)
- C_{pw} is the specific heat capacity of the wall (J/kgK)
- h_f is convective heat transfer coefficients from solid to gas (W/m^{2}K)
- h_w is convective heat transfer coefficients from gas to wall (W/m^{2}K)
- h_∞ is convective heat transfer coefficients from wall to environment (W/m^{2}K)
- d_i is the column internal diameter (m)
- t_w is the wall thickness (m)
- u is the interstitial gas velocity (m/s)

3.1.3. Momentum balance

Pressure drop during adsorption and desorption steps in a packed bed is calculated using Ergun's equation [57]:

$$\frac{\partial P}{\partial z} = 150\frac{\mu}{d_p^2}\frac{(1-\varepsilon)^2}{\varepsilon^2}u + 1.75\frac{\rho}{d_p}\frac{(1-\varepsilon)}{\varepsilon}u^2 \tag{3.7}$$

where u_0 is a superficial velocity, d_p is an adsorbent partice diameter and μ is a viscosity. The equation 3.7 is valid for the Reynolds number range between 1 and 10^4 [58]. The velocity is assumed to be constant.

The pressurization modelling approach varies depending on the gas composition. An approach for modelling the pressurization of an isothermal packed bed with inert gas is provided by Rodrigues et al. [59]. Assuming the isothermal bed, the Continuity equation can be rearranged using the Ideal Gas Law (see Appendix A.6):

$$\frac{\partial P}{\partial t} = -u\frac{\partial P}{\partial z} - P\frac{\partial u}{\partial z} \tag{3.8}$$

The velocity, involved in equation 3.8, can be derived from Ergun's equation 3.7:

$$u = \frac{-a + \sqrt{a^2 - 4b(M/RT)P\frac{\partial P}{\partial z}}}{2b(M/RT)P} \tag{3.9}$$

where

$$a = 150\frac{\mu}{d_p^2}\frac{(1-\varepsilon)^2}{\varepsilon^3} \tag{3.10}$$

and

$$b = 1.75\frac{\rho}{d_p}\frac{(1-\varepsilon)}{\varepsilon} \tag{3.11}$$

Then derivative of velocity with respect to z:

$$\frac{\partial u}{\partial z} = \frac{a + \sqrt{a^2 - 4b(M/RT)P\frac{\partial P}{\partial z}}}{2b(M/RT)}\frac{1}{P^2}\frac{\partial P}{\partial z} - \frac{1}{P}\frac{P\frac{\partial^2 P}{\partial z^2} + \left(\frac{\partial P}{\partial z}\right)^2}{\sqrt{a^2 - 4b(M/RT)P\frac{\partial P}{\partial z}}} \tag{3.12}$$

The equation 3.8 can be rearranged using equations 3.9 and 3.12:

$$\frac{\partial P}{\partial t} = \frac{P\frac{\partial^2 P}{\partial z^2} + \left(\frac{\partial P}{\partial z}\right)^2}{\sqrt{a^2 - 4b(M/RT)P\frac{\partial P}{\partial z}}} \tag{3.13}$$

The resulting equation 3.13 is a partial differential equation, which describes the change of pressure in space and time.

Rodrigues et al [59] also describe the modelling approach for fixed bed pressurization with a binary mixture of inert and active i.e. adsorbable gases. The coupled partial differential equations should be solved to track the variations in pressure and mole fraction throughout time and space:

$$\frac{\partial P}{\partial t} = -u\frac{\partial P}{\partial z} - P\frac{\partial u}{\partial z} - \left(\frac{1-\varepsilon}{\varepsilon}\right)\rho_s\frac{\partial q_1}{\partial t}RT \tag{3.14}$$

$$\frac{\partial y_1}{\partial t} = D_L\left(\frac{\partial^2 y_1}{\partial z^2} - \frac{1}{P}\frac{\partial y_1}{\partial z}\frac{\partial P}{\partial z}\right) - u\frac{\partial y_1}{\partial z} - \left(\frac{1-\varepsilon}{\varepsilon}\right)\rho_s\frac{\partial q_1}{\partial t}RT \tag{3.15}$$

where index 1 denotes the adsorbable component i.e. active component in a binary mixture. The derivation of equations 3.14 and 3.15 can be found in Appendix A.7. Upon comparing equations 3.8 and 3.14, it can be observed that the first two terms on the right-hand side of equation 3.14 and the right-hand side of equation 3.8 are identical. Therefore, the final form of the coupled partial differential equations is as follows:

$$\frac{\partial P}{\partial t} = \frac{P\frac{\partial^2 P}{\partial z^2} + \left(\frac{\partial P}{\partial z}\right)^2}{\sqrt{a^2 - 4b(M/RT)P\frac{\partial P}{\partial z}}} - \left(\frac{1-\varepsilon}{\varepsilon}\right)\rho_s\frac{\partial q_1}{\partial t}RT \tag{3.16}$$

$$\frac{\partial y_1}{\partial t} = D_L\left(\frac{\partial^2 y_1}{\partial z^2} - \frac{1}{P}\frac{\partial y_1}{\partial z}\frac{\partial P}{\partial z}\right) - u\frac{\partial y_1}{\partial z} - \left(\frac{1-\varepsilon}{\varepsilon}\right)\rho_s\frac{\partial q_1}{\partial t}RT \tag{3.17}$$

3.2. Input parameters

In this section, an overview is provided regarding the necessary input data for the determination of process variables.

3.2.1. Porosity

Benyahia et al. [60] propose the mean bed porosity estimation as a function of the ratio between adsorbent particle diameter (d_p) and adsorption column diameter (d_in). The following relationship holds for spherical particles:

$$\varepsilon_m = 0.39 + \frac{1.74}{(d_{in}/d_p + 1.14)^2} \tag{3.18}$$

The previous equation covers the d_{in}/d_p range of 1.5 to 50.

In the model, a uniform bed porosity distribution is assumed. However, it is possible for the bed porosity density to be lower close to the wall. This lower porosity density can lead to higher velocities near the wall, which can disrupt the plug flow behaviour typically assumed in idealized models. This phenomenon is referred to as channelling. To mitigate channelling and promote more uniform flow distribution, it is recommended to maintain a bed diameter-to-adsorbent particle ratio (d_{in}/d_p) equal to or higher than 20 [61].

3.2.2. Velocity

The velocity contributes to the advection term in the mass and energy balance equations. The superficial velocity can be determined by dividing the known feed mass flow rate, represented as $\dot{m}_{feed}$, by the cross-sectional area of the adsorption column and feed density. The diameter of the column, denoted as d_t, is used to calculate this area:

$$u_s = \frac{\dot{m}_{feed}}{\rho_{feed} A_c} \tag{3.19}$$

where u_s is superficial velocity. The relationship between superficial velocity and interstitial velocity is expressed as follows:

$$u = \frac{u_s}{\varepsilon} \tag{3.20}$$

During the adsorption and desorption steps, it is assumed that the velocity remains constant. However, this assumption does not hold true for the pressurization and depressurization steps, where the flow gradually becomes stagnant. As the flow approaches stagnation, the velocity decreases and eventually approaches zero.

In the context of pressurization and depressurization, the velocity can be described using either Darcy's law or Ergun's equation. Darcy's law relates the velocity to the pressure gradient and the permeability of the porous medium. On the other hand, Ergun's equation incorporates both the viscous and frictional effects of the fluid flow through a packed bed. Both equations provide a means to estimate the velocity under different flow conditions encountered during the pressurization and depressurization steps. The expression for velocity derived from Darcy's equation can be summarized as follows:

$$u = -\frac{K}{\varepsilon \mu} \frac{\partial P}{\partial z} \tag{3.21}$$

where K is a permeability. For estimating permeability, Narasimhan et al.[62] recommend the following equation:

$$K = \frac{\varepsilon^3}{(1-\varepsilon)^2} \frac{d_p^2}{150} \tag{3.22}$$

It needs to be highlighted that Darcy's law for laminar flows with Reynolds number up to 10 [63]. The wider range of Reynolds numbers, namely from 1 to 10^4, numbers covered by the Ergun equation [58]. Therefore it is preferred to obtain velocity from Ergun's equation rather than Darcy'equation.

3.2.3. Effective thermal conductivity

The effective thermal conductivity of porous packed beds with uniform spherical particles refers to the overall thermal conductivity of the bed, considering the combined influence of both the solid particles and the void spaces between them. Zehner and Schlunder [64] proposed a correlation to estimate the effective thermal conductivity, which can be expressed as follows:

$$\frac{k_{eff}}{k_g} = 1 - \sqrt{1-\varepsilon} + \frac{2\sqrt{1-\varepsilon}}{1-\lambda B} \left(\frac{(1-\lambda)B}{(1-\lambda B)^2} \ln\left(\frac{1}{\lambda B}\right) - \frac{B+1}{2} - \frac{B-1}{1-\lambda B} \right) \tag{3.23}$$

where

$$B = 1.25 \left(\frac{1-\varepsilon}{\varepsilon} \right)^{10/9} \tag{3.24}$$

and

$$\lambda = \frac{k_g}{k_s} \tag{3.25}$$

k_g and k_s are thermal conductivities of gas and solid phases respectively.

3.2.4. Convective heat transfer from gas to wall

The relationship between the Nusselt number and the Reynolds number is required for analyzing the forced convection inside the column. The specific equation representing this relationship is provided as follows [65]:

$$Nu_w = 0.813Re^0.19e^{-6d_p/d_i} \tag{3.26}$$

3.2.5. Convective heat transfer from wall to environment

The external convective heat transfer coefficient can be calculated from the Nusselt number [66]:

$$Nu_\infty = \left(2 + \frac{0.387Ra^{1/6}}{(1+(0.492/Pr)^{9/16})^8/27}\right)^2 \tag{3.27}$$

3.2.6. Loading

The three phases that make up the adsorption mechanism are: 1. external (or film) mass transfer of solute molecules from the solution bulk to the sorbent particle surface; 2. diffusion through the internal structure of the particle to the sorption sites; and 3. fast absorption. Film mass transfer and interparticle diffusion continue to be the rate-determining phases because Step 3 is infinitely rapid and provides no resistance to the adsorption process [67]. In order to ease the computational cost, the mass transfer resistances are lumped into a single parameter and loading is expressed as a linear relationship [51]:

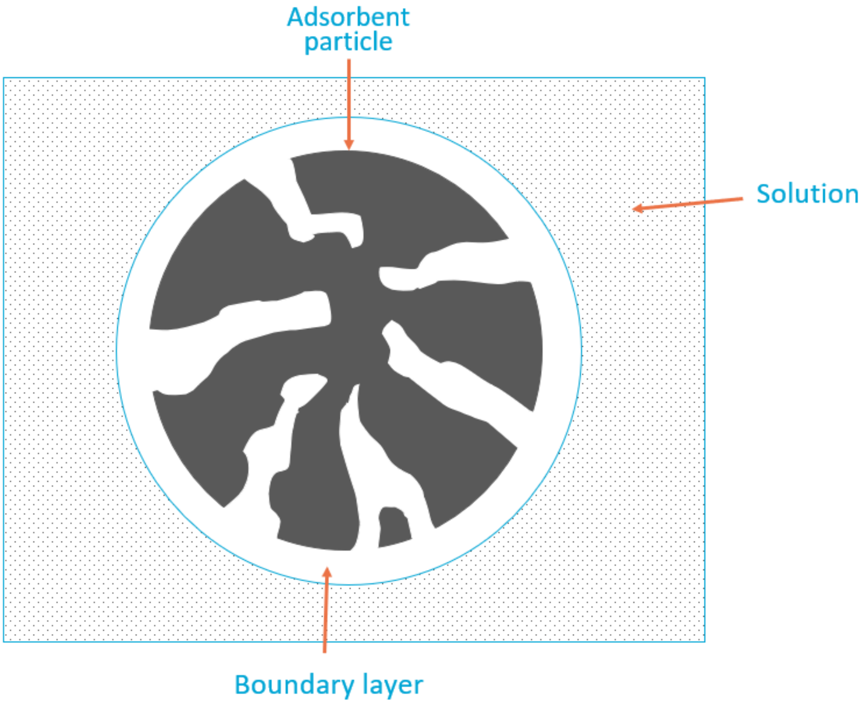

Figure 3.2: Sketch of an adsorbent particle in solution

$$\frac{\partial q_i}{\partial t} = k_{LDF}(q_i^{eq} - q_i) \tag{3.28}$$

where k_{LDF} is a linear driving force constant. The equation 3.28 is known as a linear driving force model and it works well in practice [68]. The equilibrium loading q_i^{eq} values are taken from adsorption isotherm models, which are based on experimental data (See the subsection 3.2.7).

3.2.7. Adsorption isotherm

In the linear driving force model, the equilibrium adsorption is obtained from adsorption isotherms discussed in Chapter 2. These isotherm models are adjusted to experimental data. The adsorption of water on zeolite 5A, 13x, and silica gel is explained using the Toth model, while the water adsorption on zeolite 3A and 4A is described by the triple-site Langmuir model. The triple-site Langmuir model parameters for silica gel are fitted to experimental data from Ref. [55]. The Toth model [37] has the following form:

$$q_i^{eq} = \frac{aP_i}{(1 + (bP_i)^t)^{1/t}} \tag{3.29}$$

the parameters a, b and t in Toth equation are described below:

$$b = b_0 \,\text{exp}(E/T) \tag{3.30}$$

$$a = a_0 \,\text{exp}(E/T) \tag{3.31}$$

$$t = t_0 + c/T \tag{3.32}$$

The triple-site Langmuir model [35] is proposed to describe water isotherm in the form of:

$$q_i^{eq} = \frac{n_{s1} b_1 P_i}{1 + b_1 P_i} + \frac{n_{s2} b_2 P_i}{1 + b_2 P_i} + \frac{n_{s3} b_3 P_i}{1 + b_3 P_i} \tag{3.33}$$

the parameters $b1$, $b2$ and $b3$ in Toth equation are described below:

$$b_1 = b_{10} \,\text{exp}(\frac{E_1}{RT}) \tag{3.34}$$

$$b_2 = b_{20} \,\text{exp}(\frac{E_2}{RT}) \tag{3.35}$$

$$b_3 = b_{30} \,\text{exp}(\frac{E_3}{RT}) \tag{3.36}$$

The fitted Toth equation and triple-site Langmuir equation parameters for water can be found in Table 3.1 and Table 3.2.

Table 3.1: The Toth equation parameters for water

Adsorbent	a_0 mol/kg · kPa	b_0 1/kPa	E K	t_0	c K
zeolite 5A	$1.106 \cdot 10^{-7}$	$4.714 \cdot 10^{-8}$	$9.955 \cdot 10^{3}$	$3.548 \cdot 10^{-1}$	$-5.114 \cdot 10^{1}$
zeolite 13X	$3.634 \cdot 10^{-6}$	$2.408 \cdot 10^{-7}$	$6.852 \cdot 10^{3}$	$3.974 \cdot 10^{-1}$	-4.199
silica gel	$1.767 \cdot 10^{2}$	$2.787 \cdot 10^{-5}$	$1.093 \cdot 10^{3}$	$-1.190 \cdot 10^{-3}$	22.13

3.2.8. Axial dispersion coefficient

The axial dispersion coefficient is a lumped parameter that encompasses various diffusion mechanisms, such as molecular diffusion, turbulence, flow splitting and rejoining around particles, Taylor dispersion, channelling, and wall effects [69, 70, 71]. Although several correlations exist for estimating the axial dispersion coefficient, none of them encompasses all diffusion mechanisms. These correlations may not consistently provide accurate predictions for the axial dispersion coefficient in practical scenarios. Thus, it is essential to adjust them using experimental breakthrough curves.

The axial dispersion coefficient can be estimated by one of the following correlations below:

Table 3.2: The triple-site Langmuir equation parameters for water

Adsorbent	n_{s1} mol/kg	b_{10} 1/bar	E_1 kJ/mol	n_{s2} mol/kg	b_{20} 1/bar	E_1 kJ/mol	n_{s3} mol/kg	b_{30} 1/bar	E_3 kJ/mol
zeolite 3A	9.37	1.26 $\cdot\, 10^{-6}$	59.75	1.06	4.67 $\cdot\, 10^{-3}$	48.37	3.35	1.15 $\cdot\, 10^{-7}$	51.42
zeolite 4A	11.28	1.36 $\cdot\, 10^{-6}$	58.61	4.06	1.87 $\cdot\, 10^{-6}$	41.40	1.74	2.62 $\cdot\, 10^{-7}$	92.98
silica gel	12.50	4.49 $\cdot\, 10^{-8}$	50.69	12.50	4.49 $\cdot\, 10^{-8}$	50.69	12.50	4.50 $\cdot\, 10^{-8}$	50.69

- Wakao and Funazkri [72]:

$$\frac{1}{Pe} = \frac{20}{ReSc} + 0.5 \tag{3.37}$$

- Edwards and Richardson [73]:

$$\frac{1}{Pe} = \frac{0.73\varepsilon}{ReSc} + \frac{1}{2\left(1 + \frac{13\cdot 0.73\varepsilon}{ReSc}\right)} \tag{3.38}$$

- Wicke [74]:

$$\frac{1}{Pe} = \frac{0.45 + 0.55\varepsilon}{ReSc} + 0.5 \tag{3.39}$$

- Ruthven [75]:

$$\frac{1}{Pe} = \frac{0.7\varepsilon}{ReSc} + 0.5 \tag{3.40}$$

- Wen and Fan [76]:

$$\frac{1}{Pe} = \frac{0.3\varepsilon}{ReSc} + \frac{0.5}{2\left(1 + \frac{3.8}{ReSc}\right)} \tag{3.41}$$

These correlations describe the axial dispersion coefficient as a function of the Peclet (Pe), Reynolds (Re), and Schmidt (Sc) numbers. The definition of Pe, Re and Sc numbers can be found below:

$$Re = \frac{\rho_f \varepsilon u d_p}{\mu} \qquad Sc = \frac{\mu}{\rho_f D_m} \qquad Pe = \frac{u d_p}{D_L} \tag{3.42}$$

Molecular diffusion is involved in all correlations through Schmidt number. The molecular diffusion can be estimated using Chapman-Enskog's equation [77]:

$$D_m = \frac{1.858 \times 10^{-7} T^{\frac{3}{2}}}{P \sigma_{ij}^2 \Omega} \left(\frac{1}{M_i} + \frac{1}{M_j} \right) \tag{3.43}$$

where σ_{ij} is the average collision diameter between molecules i and j, which is defined as follows [78]:

$$\sigma_{ij} = \frac{1}{2}(\sigma_i + \sigma_j) \tag{3.44}$$

$$\sigma_i = 0.841 V_c^{1/3} \tag{3.45}$$

Ω is the temperature-dependent collision integral:

$$\Omega = [44.54(k_B T/\epsilon_{i,j})^{-4.909} + 1.911(k_B T/\epsilon_{i,j})^{-1.575}]^{0.1} \tag{3.46}$$

where $\epsilon_{i,j}$ is effective Lennard-Jones parameter for a mixture of molecules i and jm which is calculated from following eqation:

$$\epsilon_{i,j} = \sqrt{\epsilon_i \epsilon_j} \tag{3.47}$$

$$\epsilon_i = 0.75 k_B T_c \tag{3.48}$$

Please note that in the above equations temperature,T in K and partial pressure$P$ in atm. M is molar mass in g/mol.

3.2.9. Linear driving force constant

The linear driving force constant is a parameter used in the linear driving force model. Existing correlations, as mentioned in the works of Ruthven [75] and Naidu and Sridhar [79], can be employed to predict the linear driving force constant. However, it is crucial to cross-check these correlations with experimental data to ensure accuracy. Table 3.3 provides the linear driving force constant values for water based on experimental data.

Table 3.3: The linear driving force constant for water [56, 80, 81]

Adsorbent	k_{LDF} 1/s
zeolite 5A	$9.8 \cdot 10^{-4}$
zeolite 13X	$4 \cdot 10^{-3}$
silica gel	$4.9 \cdot 10^{-3}$

3.3. Numerical approach

Process variables are represented by a system of non-linear partial differential equations (PDEs). The method of lines is a computational technique used to solve PDEs by discretizing all dimensions except one [82]. This approach enables the conversion of a system of PDEs into a system of ordinary differential equations (ODEs), which can be solved using available integration schemes for ODEs. The Finite Difference method [83] is chosen for spatial discretization due to its simplicity of implementation. First-order upwind and second-order central difference schemes are used for spatial discretization:

$$f^{'}(i) = \frac{f(i+1) - f(i)}{\Delta z} \tag{3.49}$$

$$f^{"}(i) = \frac{f(i+1) - 2f(i) + f(i-1)}{\Delta z^2} \tag{3.50}$$

Boundary conditions are imposed via ghost cells. Ghost cells are additional cells added at both ends of the main computational domain to provide information about the values at the boundaries. The boundary conditions at the inlet are established based on the feed conditions. This implies the application of Dirichlet boundary conditions. The constant feed conditions assumption means the time derivative of the variable at the first ghost point equals zero.

$$\left.\frac{\partial f}{\partial t}\right|_i = 0 \tag{3.51}$$

Adsorption does not occur at the edge, just before the outside of the column. Consequently, the change in time at the boundary is equal to the change in the previous node. This condition is known as the Neumann boundary condition.

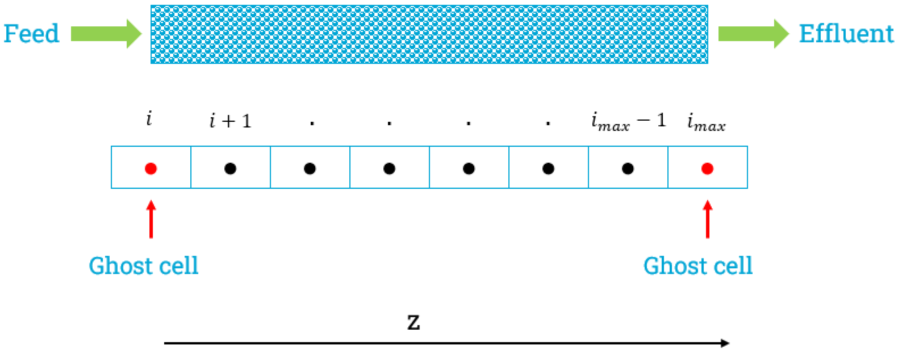

Figure 3.3: Spatial discretization

$$\left.\frac{\partial f}{\partial t}\right|_{i_{max}} = \left.\frac{\partial f}{\partial t}\right|_{i_{max}-1} \tag{3.52}$$

During adsorption and desorption the equations 3.1, 3.4, 3.5, 3.6 and 3.28 are solved between nodes $i+1$ and $i_{max}-1$. A general representation of spatial discretization and boundary conditions can be seen in Figure 3.3.

The mass and energy balance equations have been discretized and implemented using Python, version 3.8 [84]. To solve the ordinary differential equations, the solve ivp function from the SciPy package [85], version 1.11.2, has been employed. The Radau integration scheme has been selected, as it is recommended for tackling stiff problems [86].

4

Results and Analysis

4.1. Model validation

The basic steps of PSA or TSA include pressurization, adsorption, depressurization, and desorption. In terms of modelling, pressurization and depressurization are described using one set of equations, while adsorption and desorption are described using another set of equations. The transition from pressurization to depressurization or from adsorption to desorption, and vice versa, is achieved by adjusting the boundary conditions. Thus, it is sufficient to validate either pressurization or depressurization, as well as either adsorption or desorption.

The model validation is performed by reproducing the works described in scientific papers. The scientific papers for modelling pressurization and adsorption will be provided in the following subsections. The scientific papers containing experimental adsorption data for the hydrogen and water system could not be found. However, in the absence of such data, the adsorption model was validated using a nitrogen and water system, wherein nitrogen serves as an inert carrier gas. This approach allows us to assess the accuracy of the modelling technique. Nevertheless, it is important to note that further validation is necessary to refine the model for the specific water and hydrogen system.

4.1.1. Pressurization with inert gas

The modelling pressurization stage is important for determining the subsequent adsorption step's initial conditions and calculating the pressurization time. The modelling fixed bed pressurization with an inert gas implies solving Equation 3.8. The velocity involved in Equation 3.8 can be derived either from Darcy's equation or Ergun's equation.

Rodrigues et al. [59] used velocity data obtained from Darcy's equation to simulate the pressurization of a 1 m long fixed bed with a porosity of 0.43, where the pressure was increased from 1 atm to 5 atm. The comparison between the numerical solution of Equation 3.8 and the results presented by Rodrigues et al. are depicted in Figures 4.1 and 4.2. The axial pressure profiles during the pressurization process are illustrated in Figure 4.1 and the corresponding axial velocity profiles can be seen in Figure 4.2. The highest velocities are observed at the beginning of the pressurization step when the pressure gradient is at its maximum. Toward the end of the pressurization step, the pressure gradient tends to approach zero. Consequently, the velocity also tends to decrease and approach zero, as there is a direct relationship between velocity and pressure gradient according to Equation 3.21. The velocity at the closed end of the fixed bed is equal to zero during pressurization. The matching comparison results suggest that the modelling approach is valid. The nature of gas utilized for pressurization and the value of permeability remain unclear since Rodrigues et al. [59] arbitrarily take K/μ proportion value equal to 0.05 $\mathrm{m}^2/\mathrm{atm} \cdot \mathrm{sec}$. Expanding the application of Rodrigues et al.'s approach to other cases is complicated by the absence of a permeability equation.

The approach in which velocity is defined through Ergun's equation is described by C.Sereno et al. [87]. C.Sereno et al simulate the pressurization of a 1.5 m long fixed bed with a porosity of 0.4, where the pressure was increased from 1 atm to 5 atm. The comparison between the model outcome and

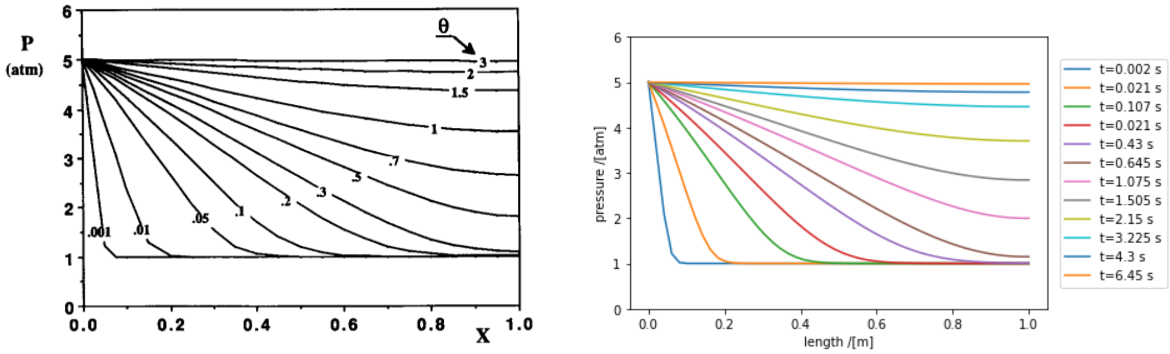

Figure 4.1: Comparison of axial pressure profiles during pressurization of an adsorption bed with an inert gas. The left side depicts the original work by Rodrigues et al.[59], while the right side shows the reproduced results. The conditions are as follows: P_l = 1 atm, P_h = 5 atm, L = 1 m, K/μ = 0.05 m²/atm·sec. The dimensionless time θ is defined as $\theta = t/\tau_c$, where τ_c is the characteristic time of 2.15 seconds. The dimensionless length x is defined as x = z / L.

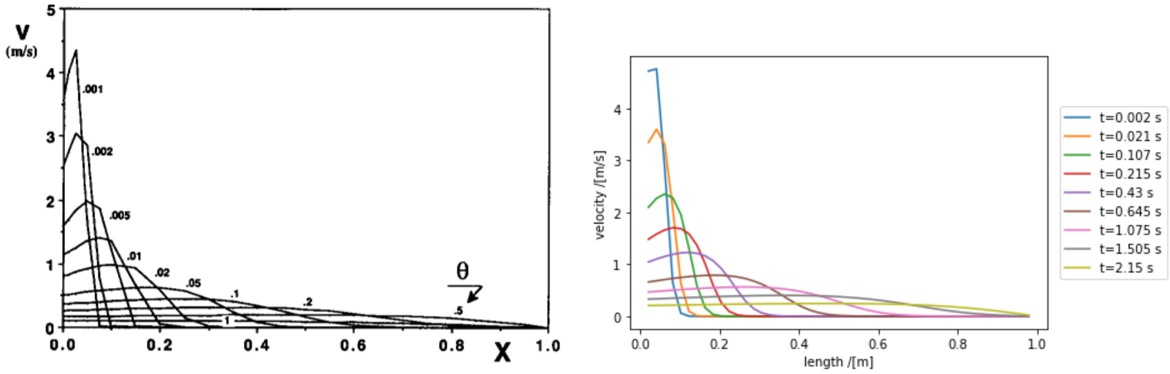

Figure 4.2: Comparison of axial velocity profiles during pressurization of an adsorption bed with an inert gas. The left side depicts the original work by Rodrigues et al. [59], while the right side shows the reproduced results. The conditions are as follows: P_l = 1 atm, P_h = 5 atm, L = 1 m,ε = 0.43, K/μ = 0.05 m²/atm·sec. The dimensionless time θ is defined as $\theta = t/\tau_c$, where τ_c is the characteristic time of 2.15 seconds. The dimensionless length x is defined as x = z / L.

results of C.Sereno et al work is depicted in Figures 4.3 and 4.4. The axial pressure profiles during pressurization are shown in Figure 4.3, whereas the axial velocity profiles can be seen in Figure 4.4. It can be concluded that C.Sereno et al. [87] work is reproduced accurately based on the comparison.

When comparing Figures 4.1 and 4.3, it is evident that the pressurization time is shorter when Ergun's equation is used instead of Darcy's equation. However, it is important to note that this section focuses on the validation of the model by reproducing the work described in scientific papers. It should be emphasized that there are differences in the fixed bed dimensions and fluid properties between the studies conducted by Rodrigues et al [59] and C. Sereno et al [87] (see Table 4.1). To conduct a sensitivity analysis on the influence of velocity definition on pressurization time, it is crucial to maintain consistent bed characteristics and fluid properties.

The pressurization time, as depicted in the models presented by Rodrigues et al. and C. Sereno et al., is relatively short due to the maintenance of a consistently high pressure at the inlet of the column throughout the entire pressurization process. In practice, it's plausible that the pressure at the inlet gradually increases, leading to a potentially longer pressurization time. It's important to note that both Rodrigues et al. and C. Sereno et al. have exclusively provided simulation results without accompanying experimental data. To validate the accuracy of the estimated pressurization time, considering the simulations presented by Rodrigues et al. and C. Sereno et al., empirical data is imperative. Experimental determination of the pressurization time involves installing pressure sensors at both the open and closed ends of the fixed bed. Full pressurization occurs when the pressures at both ends of the

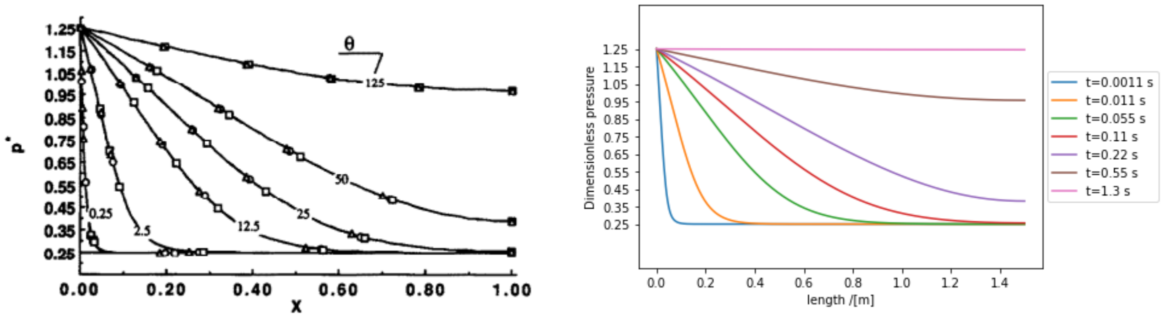

Figure 4.3: Comparison of axial pressure profiles during pressurization of an adsorption bed with an inert gas. The left side depicts the original work by C. Sereno et al [87], while the right side shows the reproduced results. The conditions are as follows: P_l = 1 atm, P_h = 5 atm, L = 1.5 m,ε = 0.4, d_p=0.0002 m, μ = 1 × 10^{-5} kg / m ·s. The dimensionless pressure $P^* = P/(P_h - P_l)$. The dimensionless time θ is defined as $\theta = t/\tau_c$, where τ_c is the characteristic time of 0.0044 seconds. The dimensionless length x is defined as x = z / L.

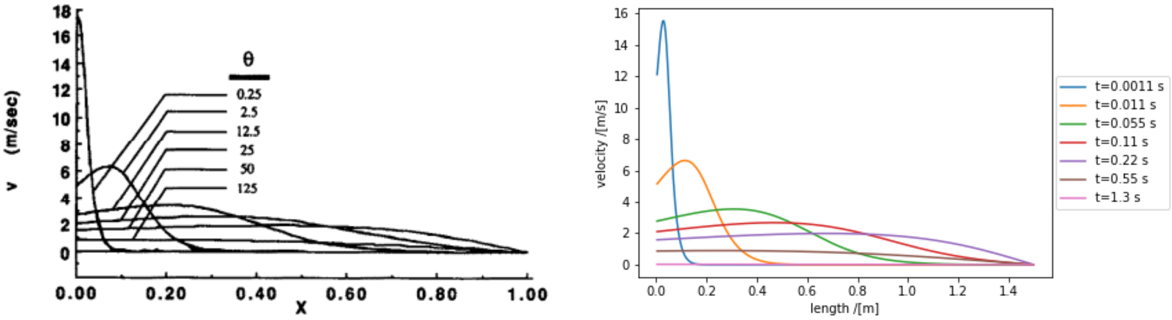

Figure 4.4: Comparison of axial velocity profiles during pressurization of an adsorption bed with an inert gas. The left side depicts the original work by C. Sereno et al. [87], while the right side shows the reproduced results. The conditions are as follows: P_l = 1 atm, P_h = 5 atm, L = 1.5 m,ε = 0.4, d_p=0.0002 m, μ = 1 × 10^{-5} kg / m ·s. The dimensionless pressure $P^* = P/(P_h - P_l)$. The dimensionless time θ is defined as $\theta = t/\tau_c$, where τ_c is the characteristic time of 0.0044 seconds. The dimensionless length x is defined as x = z / L.

fixed bed reach equilibrium.

Table 4.1: Input data used in pressurization models by Rodrigues et al. [59] and Sereno et al. [87]. The key distinction between models lies in velocity definitions. Rodrigues et al. [59] derive velocity using Darcy's equation, while Sereno et al. [87] derive velocity based on Ergun's equation.

Parameters	Rodrigues et al. [59]	Sereno et al. [87]
Bed length (m)	1	1.5
Porosity	0.43	0.4
Particle diameter (m)		0.0002
Viscosity (kg / m ·s)		1 × 10^{-5}

4.1.2. Pressurization with a mixture of inert and adsorbable gases

In the case of fixed-bed pressurization with a feed containing inert and adsorbable gases, the adsorption capacity of the bed decreases due to adsorption during pressurization. The pressurization process with a mixture of inert and adsorbable gases should be modelled to account for this reduction in adsorption capacity.

According to Rodrigues et al. [59], the modelling fixed-bed pressurization with a binary mixture of inert and adsorbable gases involves solving coupled partial differential Equations 3.16 and 3.17. This approach necessitates input data such as the axial dispersion coefficient, adsorption isotherm, and loading. In their work, Rodrigues et al. [59] provide the axial dispersion coefficient and adsorption isotherm. However, they introduce an alternative technique, distinct from the conventional linear driving force model, for describing the change in loading over time ($\frac{\partial q}{\partial t}$). Unfortunately, the details of this alternative approach are unclear, making it challenging to accurately reproduce their work. Consequently, the specific method for determining the change in loading remains ambiguous, hindering the replication of their findings.

Table 4.2: Input data for fixed bed pressurization models. The difference between models lies in the gas composition used for fixed bed pressurization.

Input parameter	Pressurization with an inert gas	Pressurization with a mixture of inert and adsorbable gases
Bed length (m)	1.5 m	1.5 m
Porosity	0.4	0.4
Particle diameter (m)	0.0002	0.0002
Viscosity (kg / m ·s)	1	1
Particle density (kg/m^3)		1350
Linear driving force coefficient (1/s)		4×10^{-5}
Axial dispersion coefficient (m^2/s)		0.465×10^{-2}
Adsorbable gas mole fraction (%)	0	1

In the absence of scientific papers and experimental data, it is not possible to validate the model of pressurization with a mixture of inert and adsorbable gases. However, the model's behaviour can be quantitatively assessed by comparing it to the already validated model of pressurization with inert gas. The downstream of the alkaline electrolyser primarily consists of hydrogen, with impurities in the form of oxygen and water vapour. It is assumed that the oxygen is completely converted into water at the deoxygenation unit located before the PSA, as shown in Figure 2.7. Therefore, the PSA feed contains water vapour and hydrogen, with the latter serving as an inert carrier gas. Considering the low water content, one can expect that the results of the model of pressurization with a gas mixture should not deviate significantly from the model of pressurization with an inert gas.

To simulate the pressurization of an adsorption column using a mixture of inert and adsorbable gases, the same column dimensions, feed pressure, and temperature are maintained, as in the case of pressurization with inert gas. A comprehensive list of model input parameters can be found in Table 4.2. Axial dispersion coefficient and linear driving force coefficient values are chosen arbitrarily. The fixed bed is assumed to consist of zeolite 3A and an adsorption isotherm is taken from Table 3.2. Pressurization with inert gas and pressurization with a mixture of inert and adsorbable gases simulations results are compared in Figures 4.5 and 4.6. As anticipated, the pressure and velocity profiles indeed exhibit identical patterns. To provide a comprehensive perspective, Figure 4.7 illustrates the variations

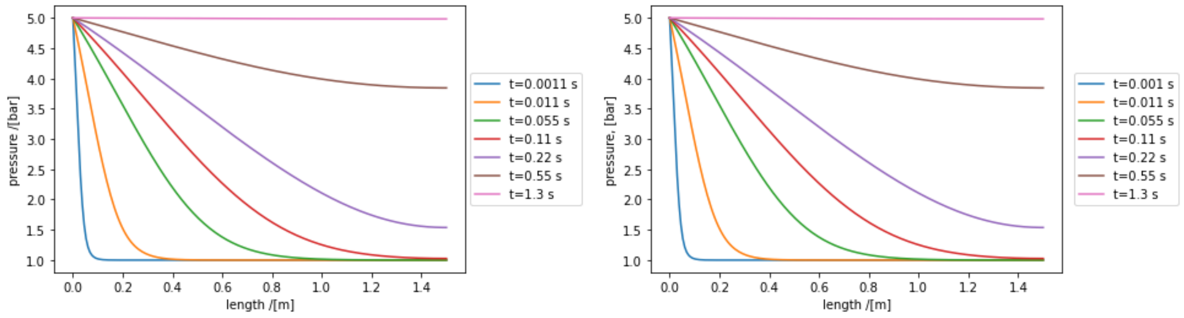

Figure 4.5: Comparison of axial pressure profiles during fixed bed pressurization. The left side depicts pressurization with inert gas, while the right side shows pressurization with a mixture of inert and adsorbable gases

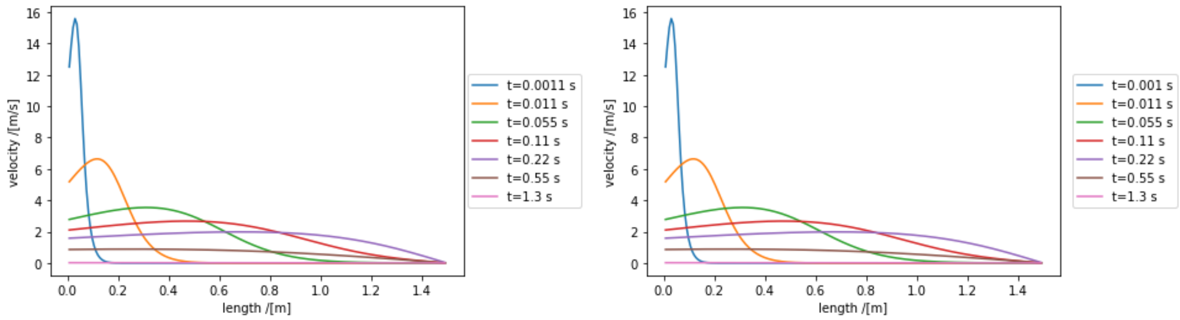

Figure 4.6: Comparison of axial velocity profiles during fixed bed pressurization. The left side depicts pressurization with inert gas, while the right side shows pressurization with a mixture of inert and adsorbable gases

in the mole fraction and loading of the adsorbable gas, referred to as the active gas. The active gas

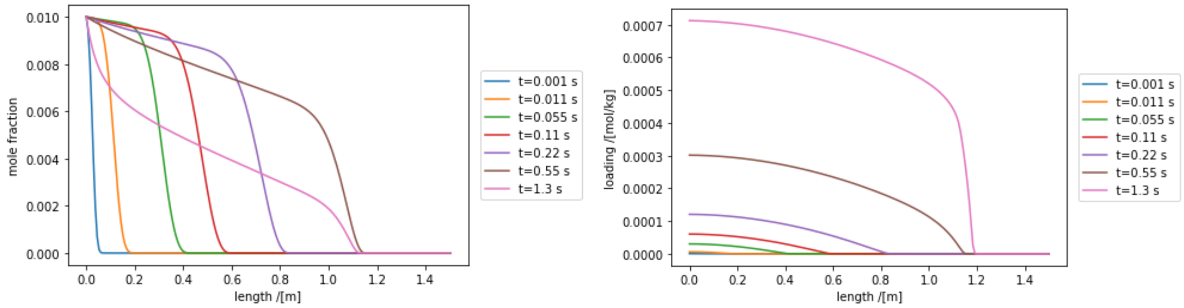

Figure 4.7: Adsorbable gas mole fraction and loading distribution during fixed bed pressurization with a mixture of inert and adsorbable gases. The left side depicts adsorbable gas mole fraction, while the right side shows adsorbable gas loading

component within the gas phase begins to disperse within the fixed bed as the pressurization process commences, reaching its maximum value at 0.55 seconds. Following this peak, the distribution of the active component within the bed starts to decrease. This phenomenon can be attributed to the transfer of the active component from the gas phase to the adsorbent, a process known as adsorption. This occurs as the flow becomes stagnant towards the end of the pressurization step and the pressure approaches its maximum value. The reduction in adsorption capacity due to pressurization with a mixture of inert and active gases is depicted on the right side of Figure 4.7. It's worth noting that the extent of this adsorption capacity reduction can increase with the higher mole fraction of the active component in the feed.

The bed volume is defined by the equation:

$$V_{\text{bed}} = A_c L = \pi \frac{d_{\text{in}}^2}{4} L \tag{4.1}$$

where A_c represents the bed's cross-sectional area, d_{in} is the inner diameter of the cylindrical column, and L denotes the bed's length. It's important to highlight that larger adsorption columns require more time to pressurize. However, it's not clear whether the influence of the bed volume is accounted for in equations 3.8 and 3.14, considering that they are one-dimensional. Equations 3.8 and 3.14 involve velocity, which can be derived from either Darcy's equation (as shown in 3.21) or Ergun's equation (as shown in 3.9). Both Darcy's and Ergun's equations necessitate the inclusion of porosity as an input parameter. Porosity, in turn, is defined by the correlation 3.18 provided by Benyahia et al. [60], which describes porosity in terms of the column's inner diameter and the diameter of the adsorbent particles. From this analysis, it can be inferred that the one-dimensional pressurization modelling approach does take into account the influence of bed volume through the incorporation of porosity in the equations. In summary, the one-dimensional modelling approach for pressurization accounts for the impact of bed volume indirectly through the consideration of porosity, as influenced by the inner diameter of the column and the size of the adsorbent particles, as described by Benyahia et al.'s correlation.

Pressurization and depressurization are important for cycle optimization but do not drastically influence the purification process. This could explain the absence of experimental data on fixed bed pressurization and depressurization in scientific papers.

4.1.3. Adsorption

Breakthrough curve analysis is used to investigate the adsorption process of solute onto an adsorbent material. It involves measuring the concentration of the solute in the effluent stream over time as it passes through the adsorption bed. The breakthrough curve typically shows an initial period where the effluent concentration is low, indicating that the adsorbent is removing the solute. However, as the adsorption capacity of the adsorbent becomes saturated, there is a breakthrough point where the effluent concentration starts to rise. This indicates that the solute is no longer being adsorbed and is being released into the effluent stream. The breakthrough curve obtained from this analysis provides valuable insights into the adsorption capacity and kinetics.

An accurate adsorption model should replicate the breakthrough curve obtained from experimental measurements. James et al. [81] describe the adsorption modelling approach and compare the model results with experimental measurements. The experiment is conducted to obtain a breakthrough curve for the water vapour and nitrogen system, where nitrogen acts as an inert carrier gas. Water concentration and gas temperature measurements are available at the midpoint and outlet of the adsorption column (see Figure 4.8).

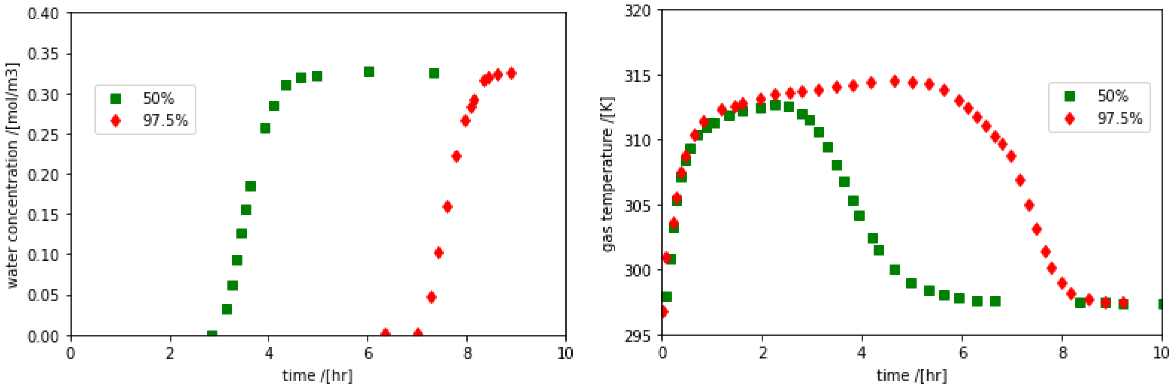

Figure 4.8: Experimental breakthrough curve obtained from testing water adsorption on Zeolite 5A [81]. Nitrogen was used as the carrier gas for this breakthrough test. The left side depicts the water concentration, while the right side shows the gas temperature. Measurements were conducted at two points within the fixed bed: the midpoint (50%) and near the exit (97.5%). Sensor locations are represented as percentages, defined as the ratio between the sensor's position and the bed's length.

James et al highlight the challenge of accurately estimating lumped variables such as axial dispersion and linear driving force coefficients using existing correlations, emphasizing the need for adjustments based on experimental data. To validate the modelling approach, it is crucial to reproduce the breakthrough curve obtained from the experiment using the same input data as specified in James et al.'s scientific paper. The complete list of input data can be found in Table 4.3. To replicate the concentration and temperature profiles measured during the experiment, solving the mass and energy balance equations mentioned in Chapter 3 is necessary. Initially, a simplified energy balance equations 3.2 and 3.3 will be applied.

Figure 4.9 shows that the model concentration prediction is well aligned with measurements, especially at the exit of the column, as a result of using axial dispersion and linear driving force coefficient already fine-tuned by James et al. However, the discrepancy in temperature between the model and measurement can be observed. The simplified energy balance model predicts that after the initial temperature spike, the temperature plateaus and remains constant until the breakthrough. Heat transfer in general occurs through advection and diffusion. The initial temperature spike in the profile predicted by the model may be attributed to these common heat transfer mechanisms. Several sensitivity cases

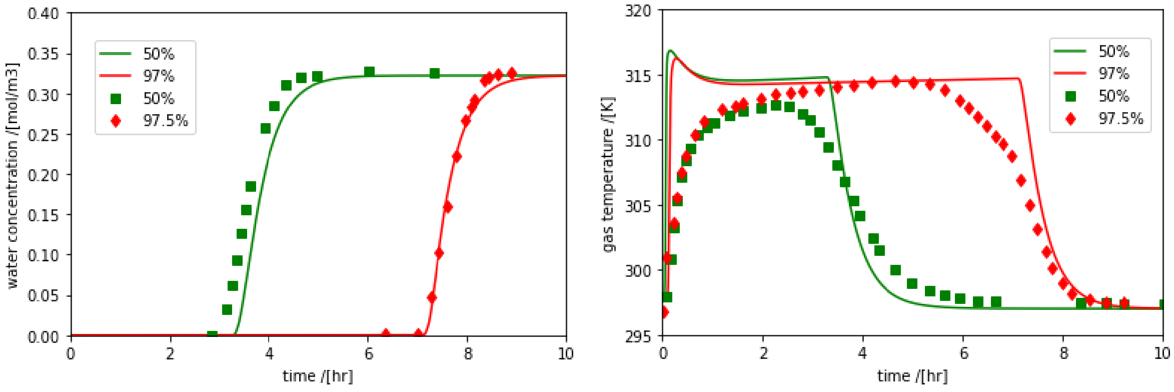

Figure 4.9: Comparison of the breakthrough curves obtained from experiment and model, which uses the simplified energy balance equations 3.2 and 3.3. The left side of the depiction represents the water concentration, whereas the right side displays the gas temperature. The experimental data is based on Ref. [81] and represented by square and diamond shaped points, while model outcome is represented by line

were run to investigate this explanation and gain a better understanding of the behaviour of the simplified energy balance model.

In Case 1 the adsorption column diameter is reduced to half of the original diameter, which results in a 4 times velocity increase in the column. The volumetric flow rate is kept constant.

$$u_0 = \frac{\dot{V}}{\varepsilon \frac{\pi}{4} d_i^2} \qquad u_1 = \frac{\dot{V}}{\varepsilon \frac{\pi}{4} (0.5 d_i)^2} = 4 u_0 \tag{4.2}$$

where u_0 and u_1 represent original and Case 1 velocities. The Case 1 results can be seen in Figure 4.10. The breakthrough takes place earlier because of increased velocity. The increase in the advection term improves heat transfer and allows it to reach a steady state faster. Therefore, there is no spike in the temperature profile in Case 1. The opposite is also true i.e. decrease in the advection term will amplify the spike in the temperature profile and delay the steady state. Case 2 with the original diameter doubled was run to prove the latter. Increasing the column diameter by a factor of two results in flow that is four times slower compared to the original velocity as shown in Equation 4.3.

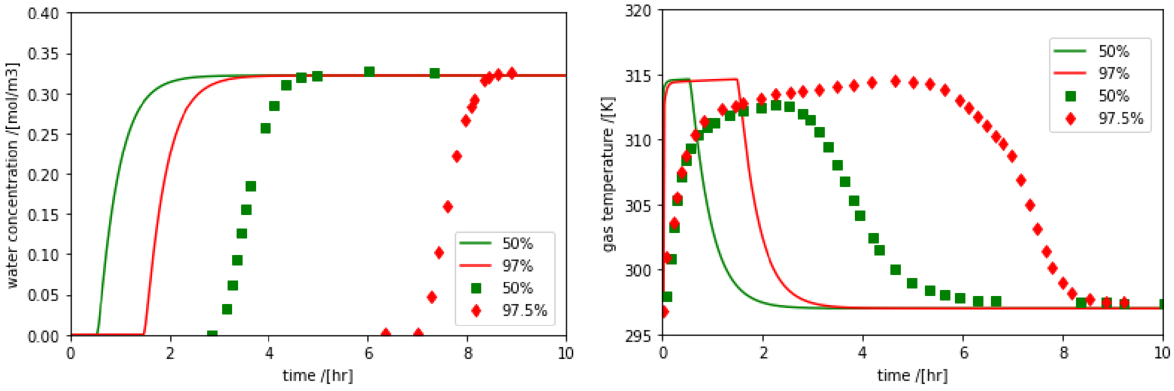

Figure 4.10: Case 1: Influence of adsorption column diameter decrease $d_{i,1}$ = 0.5 $d_{i,0}$ on concentration and temperature profiles.$d_{i,0}$ is adsorption column original diameter. The left side of the depiction represents the water concentration, whereas the right side displays the gas temperature. The experimental data is based on Ref. [81] and represented by square and diamond shaped points, while the model outcome is represented by line

$$u_0 = \frac{\dot{V}}{\varepsilon \frac{\pi}{4} d_i^2} \qquad u_2 = \frac{\dot{V}}{\varepsilon \frac{\pi}{4} (2 d_i)^2} = \frac{u_0}{4} \tag{4.3}$$

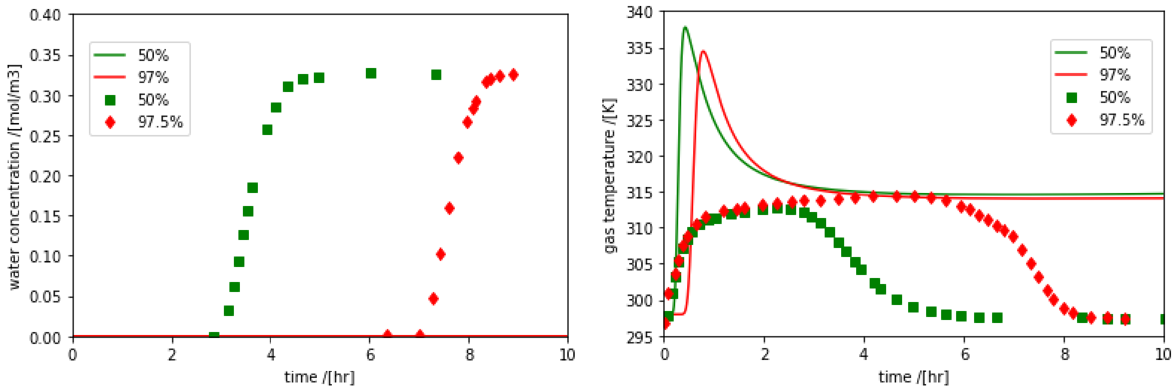

Figure 4.11: Case 2: Influence of adsorption column diameter increase $d_{i,1}$ = 2 $d_{i,0}$ on concentration and temperature profiles. $d_{i,0}$ is adsorption column original diameter. The left side of the depiction represents the water concentration, whereas the right side displays the gas temperature. The experimental data is based on Ref. [81] and represented by square and diamond shaped points, while the model outcome is represented by line

where u_0 and u_2 represent original and Case 2 velocities. As it can be seen in Figure 4.11, the breakthrough is not taking in the first 10 hours of simulation because of flow slowing down. And as was predicted the temperature increases significantly due to the advection term, which helps to dissipate the heat, reduction. Although the simplified energy balance model behaviour was explained, the fact is that the model does not accurately reproduce the temperature profiles observed in the experiment. This is because adsorption is an exothermic reaction, resulting in heat generation within the solid adsorbent particles. Then the heat is then transferred from the solid adsorbent particles to the gas until thermal equilibrium is achieved, which implies that the gas and solid particle temperatures become equal. In the experiment, the increasing gas temperature over time indicates that thermal equilibrium between the gas and solid particles was not reached during the test. To account for this, separate energy balances for the gas and solid adsorbent particles are required.

To validate this point, the model with an extended energy balance was executed. The extended energy balance model predicts more realistic temperature profiles compared to simplified energy balance as can be seen in Figure 4.12. In conclusion, the preference for the extended energy balance over the

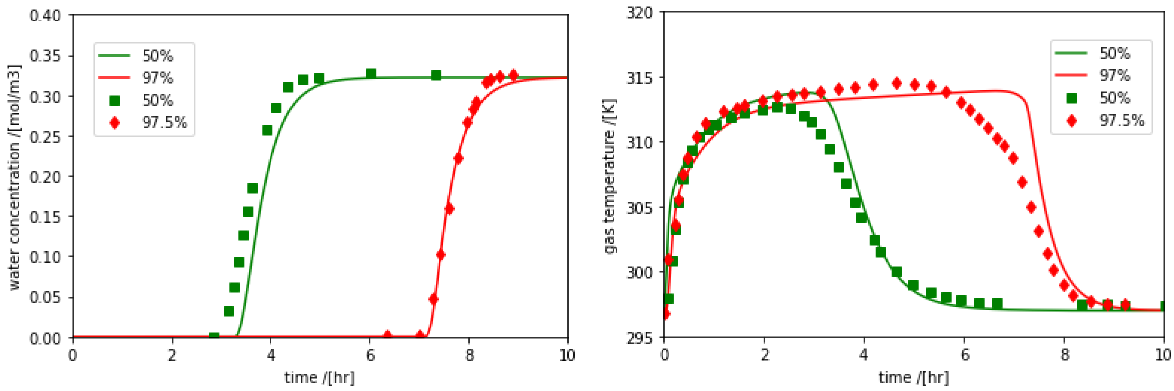

Figure 4.12: Comparison of the breakthrough curves obtained from experiment and model with an extended energy balance. The left side of the depiction represents the water concentration, whereas the right side displays the gas temperature. The experimental data is based on Ref. [81] and represented by square and diamond shaped points, while the model outcome is represented by line

simplified energy balance arises from its ability to realistically reproduce temperature changes in the fixed bed.

Table 4.3: Input data for an adsorption model reported by James et al. [81].

Feed Conditions	Initial Conditions	Bed characteristics
P_{feed}=1.056 bar	T_{gas} (x, t=0) = 297 K	L = 0.254 m
T_{feed}=297 K	T_{solid} (x, t=0) = 297 K	ε = 0.33
C_{H2O}=0.326 mol/m^3	q_{H2O} (x, t=0) = 297 K	d_i = 47.6 mm
	T_{air} (x, t) =297 K	t_{wall} = 1.59 mm
Gas, Adsorbent and Wall material properties	**Heat and Mass Transfer parameters**	
d_p = 2.32 mm	h_∞ =1.685 W/m$^2 \cdot$ K	u = 0.85 m/s
ρ_s = 1180 kg/m^3	h_f = 120 W/m$^2 \cdot$ K	D_l = 2.4 $\times$ 10^{-3} m^2/s
ρ_w = 7833 kg/m^3	h_w = 13.78 W/m$^2 \cdot$ K	k_{LDF} = 8 $\times$ 10^{-4} 1/s
ρ_g = 1.205 kg/m^3	$\Delta\ H_{H2O}$ =66 $\times$ 10^3 J/mol	
$C_{p,s}$ = 920 J/ kg $\cdot$ K		
$C_{p,w}$ = 475 J/ kg $\cdot$ K		
$C_{p,g}$ = 1041.43 J/ kg $\cdot$ K		
k_s = 3.3 W/m $\cdot$ K		
k_w = 14.2 W/m $\cdot$ K		
k_g = 0.026 W/m $\cdot$ K		
μ_g = 1.77 $\times$ 10^{-5} Pa $\cdot$ s		

4.2. Sensitivity analysis

Designing a PSA system involves selecting adsorbent material, adsorption column size and the number of columns taking into account PSA system performance and cost [88]. Adsorption column size is determined by the diameter and length. The increase in adsorption column size leads to an increase in cost due to the increase in the mass of adsorbent hold in the adsorption column and the mass of adsorption column wall material. The bed diameter influences flow velocity. The low velocity provides longer residence time, whereas high velocity helps to dissipate better the heat generated during adsorption via advection term [54]. The longer the adsorption bed, the more adsorbent it contains, which allows longer adsorption time before switching to desorption. On the other hand, the long bed leads to higher pressure drop and cost. Adsorption is an exothermic process, whereas desorption is an endothermic process. The heat generation in adsorption is undesirable since water loading decreases with temperature as shown in Figure 3.1. The heat is dissipated to the environment through the adsorption column wall. The heat consumption in desorption leads to a temperature drop which might cause ice formation if the gas temperature drops below 0°C. The heat is supplied via the adsorption column wall to enhance bed regeneration and avoid ice formation. Another aspect to consider in temperature management is the heating up of adsorption column wall material. The XINTC recommended 80°C as a wall temperature limit which is based on material manufacture recommendations. The heat of adsorption depends on the adsorbent material and the gas being adsorbent. The adsorbent material also affects the bed adsorption capacity.

The PSA system consists of 2 columns as shown in Figure 4.13. The binary mixture of the hydrogen and water vapour is fed to the adsorption column where water vapour is retained and the hydrogen with higher purity is obtained at column exit. Part of the produced pure hydrogen is diverted to the second column for bed regeneration. The hydrogen flow in the second column reduces water partial pressure which triggers desorption and carries out the water released from the adsorbent. The downstream of the column undergoing bed regeneration is called a purge. The adsorption operation in the first column is stopped before the complete bed saturation to prevent product contamination because of the S-shaped flow propagation front in the bed. Then the feed is diverted to the second column while the first

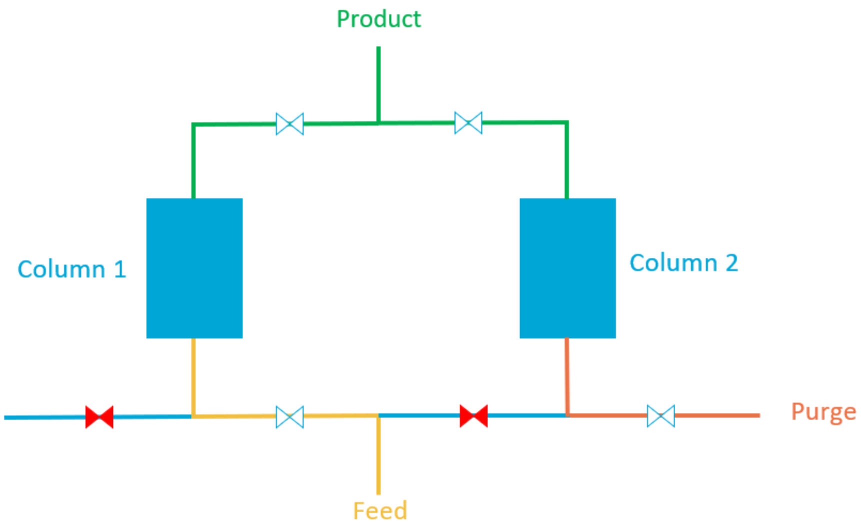

Figure 4.13: PSA configuration

column is regenerated. Adsorption and desorption are switched between columns in cyclic operation. Equal adsorption and desorption times are preferable to maintain continuous hydrogen processing in a PSA consisting of two columns. In case bed regeneration takes a longer time compared to adsorption, increasing the number of columns can be considered. An increase in the number of columns requires scheduling adsorption and desorption in cyclic operation. It also results in a cost rise due to additional adsorbent material use and heat supply in the prolonged desorption step.

The PSA performance is assessed based on key performance indicators (KPI) such as product purity, recovery and total productivity [42, 89]. The definitions of these KPIs are outlined below:

$$\text{purity} = \frac{N_{\text{H2, prod}}}{N_{\text{H2, prod}} + N_{\text{H2O, prod}}} = \frac{N_{\text{H2, prod}}}{N_{\text{prod}}} \tag{4.4}$$

$$\text{recovery} = \frac{N_{\text{H2, prod}} - N_{\text{H2, purge}}}{N_{\text{H2, feed}}} \tag{4.5}$$

$$\text{total productivity} = \frac{N_{\text{prod}} - N_{\text{purge}}}{t_{\text{cycle}} w_{\text{ads}}} \tag{4.6}$$

where $N_{\text{H2, feed}}$, $N_{\text{H2, prod}}$ and $N_{\text{H2, purge}}$ represent the cumulative hydrogen moles in feed, product and purge respectively, t_{cycle} denotes the total cycle time and w_{ads} stands for adsorbent mass. $N_{\text{H2, feed}}$ and $N_{\text{H2, prod}}$ are equal since hydrogen is assumed to be an inert gas in the model. The cumulative number of hydrogen moles in the product and purge is calculated by integrating the molar flow rate,$\dot{n}_{\text{H2}}$, leaving the column in the adsorption and desorption steps:

$$N_{\text{H2,prod}} = \int_0^{t_{ads}} \dot{n}_{\text{H2, prod}} dt \tag{4.7}$$

$$N_{\text{H2,purge}} = \int_0^{t_{des}} \dot{n}_{\text{H2, purge}} dt \tag{4.8}$$

The cumulative water moles in the product,$N_{\text{H2O, prod}}$, and purge ,$N_{\text{H2O, purge}}$, are calculated in the same way. XINTC requested to maintain recovery between 85 % and 90 %. Recovery shows the product loss due to product consumption for bed regeneration. However, in the current system, the recycle purge will be sent back to atmospheric storage, serving as a buffer for the compression step. However, the level of regeneration in subsequent cycles depends on regeneration pressure. KPI should be determined after the first cycle as prolonged adsorption in the first cycle result in misleading performance.

The cumulative amount of product, $N_{\mathrm{H2,\,prod}}$, increases with the increase of adsorption time. Adsorption time depends on bed regeneration level. In its turn, bed regeneration depends on regeneration pressure. Regeneration pressure influences heat consumption in the desorption process and determines the required heat input to prevent ice formation and passing the wall temperature threshold. The objective of sensitivity analysis is to determine the column size and bed regeneration conditions that correspond to an optimal balance between productivity and required energy input. Cost is not included as an optimisation objective, but it is indirectly involved through heat input and mass of adsorbent in total productivity equation 4.6. The first step in the optimization process is to assume bed size. In the second step bed regeneration pressure is determined. The gas and wall temperature profiles should be checked in the following step. The temperature can be controlled by supplying heat and decreasing the bed diameter. The optimization process can be repeated for different adsorbent materials. In this sensitivity analysis comparison between zeolite and silica gel is provided.

Feed with a mass flow rate of 0.0046 kg/s is supplied at a pressure of 15 bar and temperature of 5°C. The feed is a binary mixture, containing hydrogen and water vapour, with a water mole fraction 0.007. The feed conditions are assumed to be constant. The adsorption column is made of pipe with both ends enclosed by flanges. ASTM and API standard pipes are used in existing hydrogen transporting pipelines [90]. Therefore, ASTM A554 TP304L pipe made of stainless steel with an inner diameter of 0.2032 m (8 inches) is chosen as an initial guess for pipe diameter. The adsorption bed length is limited by container size since XINTC electrolysers and hydrogen post-processing equipment come as containerised units. Hence bed length can be up to 2 m.

4.2.1. Zeolite

Water loading on adsorbent depends on pressure and temperature. Bed regeneration in PSA is achieved by manipulating total pressure and mole fraction. After the adsorption steps the column is de-pressurized and in the following step, pure hydrogen with a water mole fraction of 5 ppm is supplied to further reduce partial pressure. The level of bed regeneration depends on the chosen regeneration pressure. An adsorption bed made of zeolite 3A regeneration under vacuum conditions is mentioned in several scientific papers [91, 92, 93]. Vacuum regeneration might be a reasonable choice considering the shape of water adsorption isotherm on zeolites in Figure 4.14. Several cases have been run to check the influence of atmospheric and vacuum conditions on PSA performance. Vacuum pressure can vary between 0.1 bar and 0.01 bar [94]. The results can be seen in Figure 4.15 and in Table 4.4.

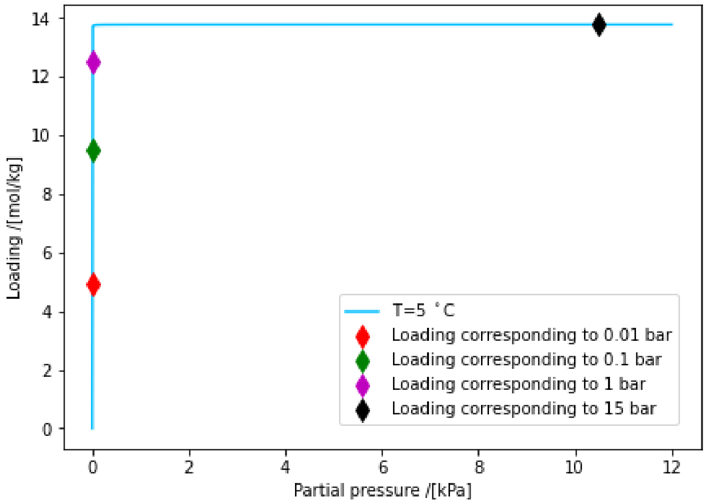

Figure 4.14: The water adsorption isotherm on zeolite 3A at a feed temperature of 5°C is described by the triple-site Langmuir model. The model parameters have been adjusted to fit experimental data, as documented in the study by Wang et al [35]. The fitted triple-site Langmuir model parameters can be found in Table 3.2

The adsorption bed is completely regenerated in the initial cycle. However, it is not feasible to reach the same level of bed regeneration at none of the considered regeneration pressures. The highest level of bed regeneration is achieved at a vacuum pressure of 0.01 bar which results in later breakthrough

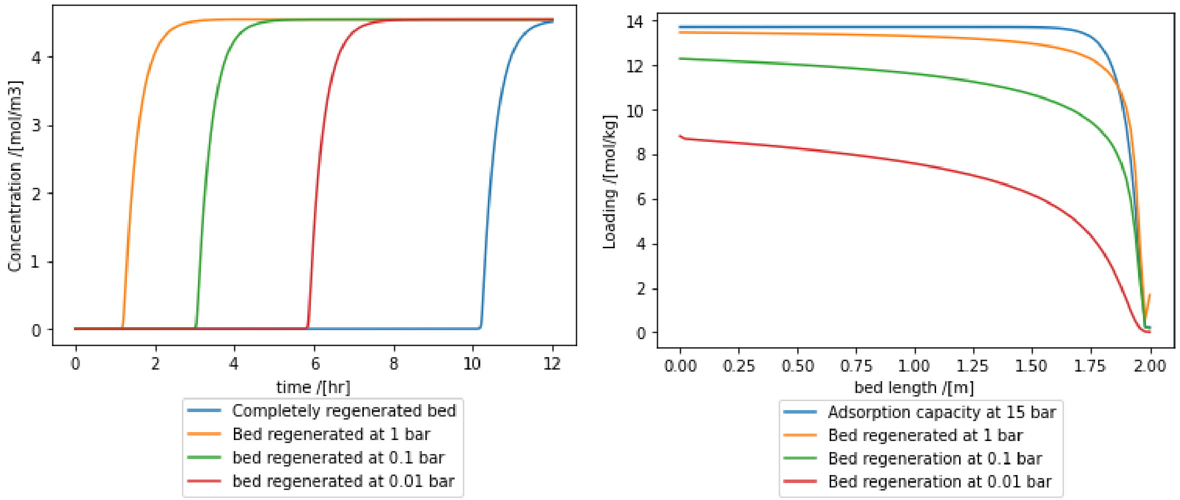

Figure 4.15: Comparison of breakthrough and useful bed capacity under various vacuum and atmospheric conditions. Useful bed capacity is defined as the difference between the loading at the end of adsorption and the loading at the end of desorption. A larger useful bed capacity leads to a longer adsorption time until breakthrough occurs.

Table 4.4: PSA performance comparison at different regeneration pressures. The heat is supplied through the outer wall of the adsorption column to maintain the gas temperature above 0°C during the desorption step.

Case	Description	Adsorbent mass (kg)	Adsorption time (hrs)	Heat input (kJ)	Purity (%)	Recovery (%)	Total Productivity (mol/hr/kg)
1	Bed regeneration at 1 bar	93.11	1.09	18.08	99.9996	85.11	35.73
2	Bed regeneration at 0.1 bar	93.11	2.97	50.21	99.99997	85.11	35.62
3	Bed regeneration at 0.01 bar	93.11	5.82	99.15	99.999996	85.11	35.54

time compared to bed regeneration at 0.1 bar and 1 bar. Recovery kept constant at 85.11 % in all cases. The heat source, assumed to maintain a constant temperature, is positioned outside the adsorption column to simulate a heat exchanger. The heat input during the desorption step is determined by integrating the heat flow over the desorption time. Purity meets ISO 14687:2019 [21] requirements in all cases. An interesting fact worth noting is that total productivity doesn't improve significantly despite extended adsorption times. To grasp this phenomenon better, it's useful to examine equation 4.6. The consistent size maintained across cases implies that the adsorbent mass also remains constant. Similarly, constant recovery signifies a stable relationship between cumulative product and cumulative purge, approximately at 0.85 $\times N_{\text{prod}}$. Therefore, the only variables changing in equation 4.6 are the total cycle time (t_{cycle}) and cumulative production (N_{prod}). As the adsorption step is prolonged, more product is indeed produced. However, there is only a slight change when productivity is evaluated per kilogram of adsorbent and per hour. The adsorption time, heat input and pressure drop become key factors in regeneration pressure selection when PSA performance is similar in all cases. The bed regenerated at 0.01 bar provides roughly 5 times longer adsorption time compared to bed regeneration at atmospheric pressure, which means less frequent column switching is needed. It is beneficial from an operational point of view since less frequent equipment use leads to longer service time. The higher heat input in Case 3 compared to Case 2 is explained by longer desorption operation. The regeneration pressure 0.01 bar is chosen considering all factors.

The operating temperature range can be checked once the regeneration pressure is selected. The gas temperature profiles during the adsorption and desorption steps can be seen in Figure 4.16. The adsorption process generates heat, however, cooling is not needed as the feed is already at a low temperature. The heat supplied during the desorption step is not sufficient to maintain a gas temperature above 0°C. The gas temperature can be raised above 0°C by increasing the heat input during the desorption step. However, this might lead to an increase in the wall temperature, surpassing 80°C,

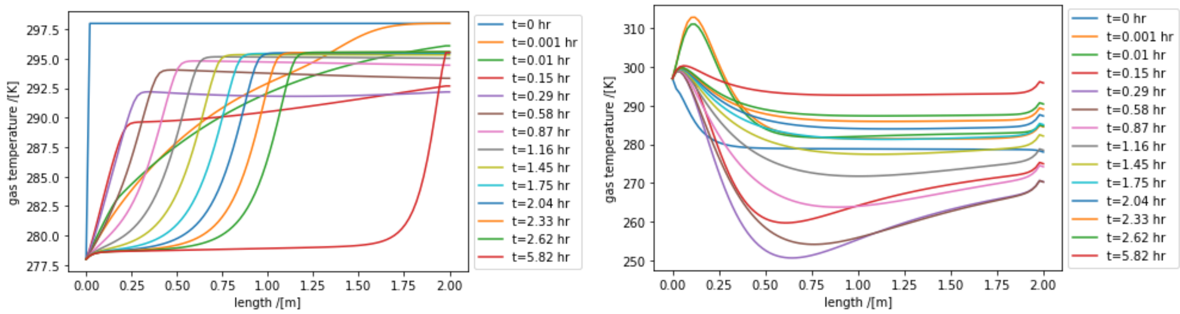

Figure 4.16: Gas temperature profiles in adsorption and desorption steps. The left side of the depiction represents the gas temperature during adsorption, whereas the right side displays the gas temperature during the desorpiton.

as heat is supplied through the wall. Another approach to enhance heat dissipation is to reduce the diameter of the adsorption column. This action increases the flow velocity, subsequently improving the advection term in the energy balance equation. The last option is to raise the feed temperature. This will result in an increase in both the gas and wall temperatures during the adsorption step, which is beneficial for the desorption step as long as the wall temperature remains below the threshold. It has been determined that the column diameter is 0.0914 m (3.6 inches) and the feed temperature 25°C keeps the gas temperature above 0°C in the desorption step after the series of iterations. The gas temperature profiles in the adsorption and desorption steps after optimization are illustrated in Figure 4.17. As can be noticed in Figure 4.17 gas temperature remains above 0°C.

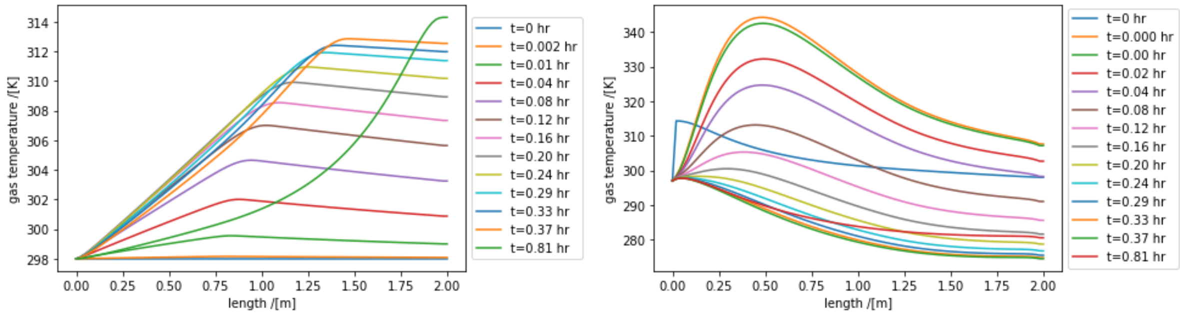

Figure 4.17: Gas temperature profiles in adsorption and desorption steps after optimization. The left side of the depiction represents the gas temperature during adsorption, whereas the right side displays the gas temperature during the desorption.

The increased velocity helped to maintain gas temperatures above 0°C in the desorption step. It also made the adsorption time shorter. The influence of change in feed conditions and adsorption column size on PSA performance can be seen in Table 4.5. The 5 times productivity improvement compared to other cases mainly is explained by the adsorbent mass decrease from 93.11 kg to 18.85 kg due to the adsorption column size reduction. The change in breakthrough time and useful bed capacity due to optimized column size and increased feed temperature can be seen in Figure 4.18.

Case 2 is considered optimal due to its sufficient adsorption time, despite the improved productivity in Case 4. The PSA system, featuring 3 columns, can be simulated once the regeneration pressure is selected, and the temperature profiles are verified. The addition of a third column allows for a desorption time twice as long as the adsorption time. This extended desorption time leads to higher levels of bed regeneration. The productivity decreased despite of better regenerated because of an increase in total adsorbent mass from 93.11 kg to 139.66 kg.

Bed regeneration at 0.1 bar is considered to be optimal based on adsorption time, thermal management and total productivity. Adding a third column is unnecessary, as it decreases productivity by increasing the total adsorbent mass. Moreover, the additional column increases costs due to the material mass required for the adsorption column and the overall increase in adsorbent mass.

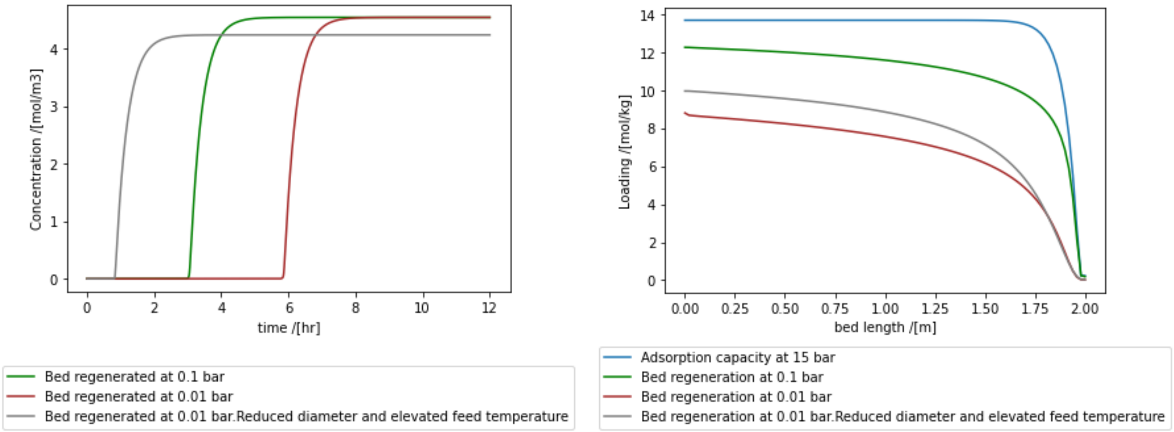

Figure 4.18: Breakthrough and useful bed capacity comparison at different atmospheric and vacuum conditions

Table 4.5: Comparison of PSA performance at different regeneration pressures. The heat is supplied through the outer wall of the adsorption column to maintain the gas temperature above 0°C during the desorption step. In case 4, the bed size and feed conditions have been adjusted to prevent ice formation during the desorption step

Case	Description	Adsorbent mass (kg)	Adsorption time (hrs)	Heat input (kJ)	Purity (%)	Recovery (%)	Total Productivity (mol/hr/kg)
1	Bed regeneration at 1 bar	93.11	1.09	18.08	99.9996	85.11	35.73
2	Bed regeneration at 0.1 bar	93.11	2.97	50.21	99.99997	85.11	35.62
3	Bed regeneration at 0.01 bar	93.11	5.82	99.15	99.999996	85.11	35.54
4	Bed regeneration at 0.01 bar. Reduced diameter and elevated feed temperature	18.85	0.81	7.31	99.999993	85.11	175.63
5	Bed regeneration at 0.1 bar. PSA with 3 columns	139.66	5.94	99.41	99.99997	85.11	23.79

4.2.2. Silica gel

The bed regeneration under vacuum conditions is unnecessary since bed regeneration at atmospheric pressure is able to reduce loading from 37 mol/kg to nearly 0 mol/kg as depicted in Figure 4.19. The adsorption time is significantly longer when compared to zeolite due to its higher adsorption capacity. The addition of an extra adsorption column into the PSA system serves the purpose of increasing the bed's useful capacity by extending the desorption time. The longer the useful bed capacity, the more extended the adsorption process becomes. It's worth noting that even without a third column, the adsorption time is already significantly long. Therefore, it can be concluded that the need for a third column is not justified.

Table 4.6: PSA performance comparison at different regeneration pressures

Case	Description	Adsorption mass (kg)	Adsorption time (hrs)	Heat input (kJ)	Purity (%)	Recovery (%)	Total Productivity (mol/hr/kg)
1	Bed regeneration at 1 bar	104.15	25.19	774.89	99.999994	90.00	33.49

The temperature profile analysis has identified a significant concern: the gas temperature drops below -50°C. This situation poses a risk of ice formation within the adsorption column, potentially leading to flow blockages. To comprehensively address the seriousness of this issue, it is essential to provide a detailed explanation of its root causes. The pure hydrogen supplied to the fixed bed reduces water

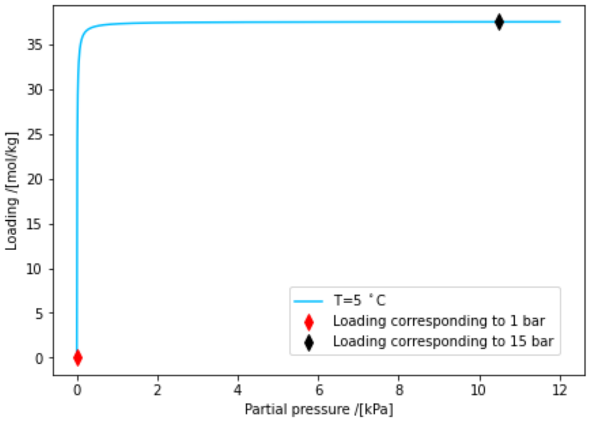

Figure 4.19: The water adsorption isotherm on silica gel at a feed temperature of 5°C is described by the triple-site Langmuir model. The model parameters have been adjusted to fit experimental data, as documented in the study by Wang et al [35]. The fitted triple-site Langmuir model parameters can be found in Table 3.2

partial pressure and triggers desorption. The water released from the adsorbent to gas is carried out towards the column exit increasing water concentration and subsequently partial pressure there. Therefore, water loading decreases at the column inlet first compared to the rest of the column as can be seen in Figure 4.20. The decrease of water loading with time, $\partial q_i/\partial t$, decreases the adsorbent temperature according to Equation 3.5. Then gas temperature decreases due to convective heat transfer between gas and adsorbent. This is how the rate of water loading change influences the gas temperature. The loading and gas temperature in Figure 4.20 are plotted at the same time interval to highlight that at the beginning of the desorption process the rate of loading higher causing a higher gas temperature drop. The extent of gas cooling depends on the heat of adsorption, heat transfer coefficients, and the difference between loading at adsorption pressure and regeneration pressure. The methods such as heat input increase, adsorption column decrease, feed temperature and purge rate increase employed in the case of zeolite did not help increase gas temperature.

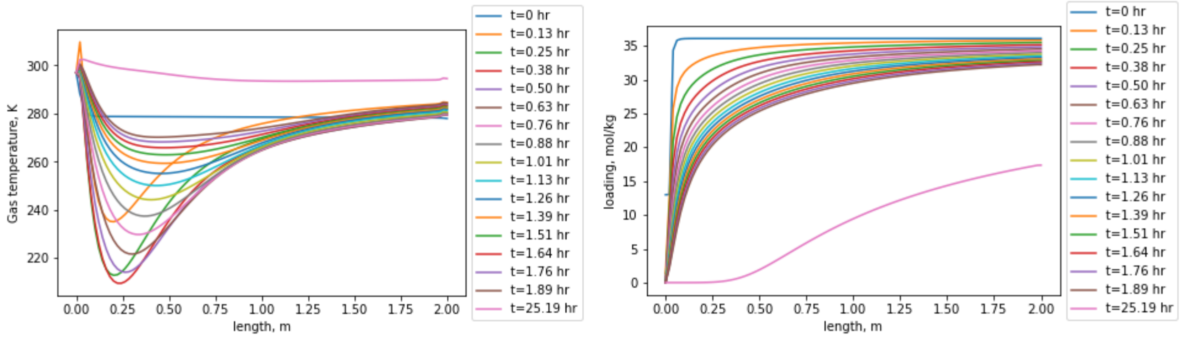

Figure 4.20: Gas temperature and loading profiles in desorption step

Adsorption favours low temperatures and high pressures. Therefore the feed is pressurized to 15 bar. Another reason for increasing feed pressure is to effectively store the product in a given volume. As can be seen in Figure 4.14 and Figure 4.19 water loading improves significantly with partial pressure increase up to 1 kPa. Change in water loading becomes negligible after a partial pressure of 1 kPa. It suggests that adsorption could be conducted below 15 bar. The pipeline between the compressor and the PSA system, and adsorption columns should be able to withstand 15 bar total pressure for safety reasons. The expenses related to the pipeline, which is able to withstand high pressure, can be reduced by performing adsorption at low pressure and putting the compressor after the PSA system.

5

Discussion

5.1. Conclusions

The hydrogen produced through alkaline water electrolysis contains impurities, including oxygen and water vapour. The goal of this project is to develop a model and design a Pressure Swing Adsorption (PSA) system aimed at reducing the water vapour content in hydrogen to meet the purity standards outlined in ISO 14687:2019.

PSA has basic four steps, namely, pressurization, adsorption, depressurization and desorption. The models for each step have been developed and validated with experimental data available in the literature. The fundamental difference in simplified and extended energy balance and its consequences have been revealed during model validation. The simplified energy balance model assumes immediate thermal equilibrium between gas and adsorbent and fails to capture realistic temperature profiles. Detailed derivations of equations involved in models can be found in the Appendix.

The design challenge primarily revolves around temperature control, despite pressure being a variable that plays a crucial role in adsorption and desorption processes. The heat release and consumption during the adsorption and desorption steps present the risk of overheating the adsorption column wall and causing ice formation. Key parameters such as diameter, feed temperature, purge rate, and heat input have been identified as tools for temperature control. The energy input required for gas compression and heat supply during the desorption step can be minimized by reducing the adsorption pressure.

In terms of the adsorbent material, a sensitivity analysis has been conducted to assess the influence of zeolite and silica gel on PSA performance. Silica gel boasts an impressive adsorption capacity of 37 mol/kg, which is 2.6 times higher than that of zeolite. This heightened adsorption capacity results in an extended adsorption time of 25 hours. From an operational perspective, this prolonged adsorption duration proves advantageous as it reduces the need for frequent column switching, ultimately extending the equipment's service life. However, there is a significant temperature drop in the gas, reaching as low as -50°C during the regeneration of the silica gel bed. Measures such as increasing heat input, decreasing the diameter, increasing the purge rate, and elevating the feed temperature did not suffice to maintain the gas temperature above 0°C.

The optimal configuration for the zeolite bed has been determined, featuring a length of 2 meters and a diameter of 0.0914 meters. This configuration has been selected based on considerations of adsorption time, productivity, and thermal operating range. It's important to note that the zeolite bed requires regeneration under a vacuum pressure of 0.1 bar, which entails additional energy input. The breakthrough time for the zeolite bed has been calculated to be 2.97 hours. In the PSA system comprising two adsorption columns, the total mass of zeolite employed is 18.85 kilograms. This configuration achieves a hydrogen purity level of 99.999% while maintaining a recovery rate of 85%. The introduction of a third column in the PSA system enables an extended bed regeneration time, which comes at the expense of reduced total productivity, decreasing from 35.62 mol/hr/kg to 23.79 mol/hr/kg due to total adsorbent mass increase from 93.11 kg to 139.66 kg.

5.2. Recommendations

The modelling approach for pressurization and depressurization has been validated, but the absence of experimental data introduces some uncertainty. The primary concern revolves around the time it takes for pressurization and depressurization. The model suggests an estimated duration of only 1 second to increase the feed pressure from 1 bar to 15 bars. This exceptionally short pressurization time may be related to how a boundary condition is imposed. Further investigation and the acquisition of experimental data are essential. In addition, pressurization and depressurization are modelled assuming an isothermal bed. In reality, the temperature might change during pressurization and depressurization due to differences between the feed and bed temperatures or the presence of adsorbable gas in the feed. Reza Haghpanah et al. [95] provide an approach for modelling fixed bed pressurization with a mixture of inert and adsorbable gases, assuming a non-isothermal bed. This modelling approach is similar to the one shown in Section 3.1.3. Transitioning from the isothermal bed assumption to the non-isothermal bed assumption should be feasible. However, it was not implemented in this work due to time constraints.

The axial dispersion coefficient and linear driving force coefficient can be approximated using correlations. Nevertheless, it is imperative to conduct experiments to validate these estimates and make adjustments if necessary. While the model's validity is confirmed through an experiment involving a binary system of nitrogen and water vapour, specific validation for hydrogen and water vapour systems is warranted. Experimental data can also contribute to accurately calculating heat transfer coefficients. The precision of these coefficients is crucial, given the design complexities associated with heating and cooling adsorption columns.

During the desorption step, heat is introduced through the outer surface of the adsorption column. However, the heat flow is constrained due to the 80°C threshold imposed on the adsorption column wall. Incorporating a heat exchanger inside the adsorption column might offer greater efficiency because it allows for direct contact with the gas and adsorbent.

The PSA design approach, design challenges, and potential solutions have been detailed in the sensitivity analysis section. Nevertheless, it is possible to structure the optimization problem more effectively and employ a more sophisticated optimization algorithm.

References

[1] John FB Mitchell. “The “greenhouse” effect and climate change”. In: *Reviews of Geophysics* 27.1 (1989), pp. 115–139.

[2] Darkwah Williams Kweku et al. “Greenhouse effect: greenhouse gases and their impact on global warming”. In: *Journal of Scientific research and reports* 17.6 (2018), pp. 1–9.

[3] “Global Energy Review 2021”. en. In: (2021).

[4] Samer Fawzy et al. “Strategies for mitigation of climate change: a review”. In: *Environmental Chemistry Letters* 18 (2020), pp. 2069–2094.

[5] United Nations. *Causes and Effects of Climate Change*. en. Publisher: United Nations. URL: `https://www.un.org/en/climatechange/science/causes-effects-climate-change` (visited on 01/26/2023).

[6] Paris Agreement. “Paris agreement”. In: *Report of the Conference of the Parties to the United Nations Framework Convention on Climate Change (21st Session, 2015: Paris). Retrived December*. Vol. 4. HeinOnline. 2015, p. 2017.

[7] United Nations. *Net Zero Coalition*. en. Publisher: United Nations. URL: `https://www.un.org/en/climatechange/net-zero-coalition` (visited on 01/26/2023).

[8] *Global Hydrogen Review 2022*. International Energy Agency, 2022.

[9] Reza Soltani, MA Rosen, and Ibrahim Dincer. “Assessment of CO2 capture options from various points in steam methane reforming for hydrogen production”. In: *International journal of hydrogen energy* 39.35 (2014), pp. 20266–20275.

[10] Jiaquan Li et al. “The carbon footprint and cost of coal-based hydrogen production with and without carbon capture and storage technology in China”. In: *Journal of Cleaner Production* 362 (2022), p. 132514.

[11] Robert W Howarth and Mark Z Jacobson. “How green is blue hydrogen?” In: *Energy Science & Engineering* 9.10 (2021), pp. 1676–1687.

[12] Hydrogen From Renewable Power IRENA. “Technology Outlook for the Energy Transition”. In: *IRENA, Abu Dhabi* (2018).

[13] “Global Energy Review: CO2 Emissions in 2021”. en. In: (2021).

[14] Mahesh Venkataraman et al. “Zero-carbon steel production: the opportunities and role for Australia”. In: *Energy Policy* 163 (2022), p. 112811.

[15] Fabrice Patisson and Olivier Mirgaux. “Hydrogen ironmaking: How it works”. In: *Metals* 10.7 (2020), p. 922.

[16] Jian Dang et al. “Hydrogen crossover measurement and durability assessment of high-pressure proton exchange membrane electrolyzer”. In: *Journal of Power Sources* 563 (2023), p. 232776.

[17] Ahmadreza Rahbari et al. “Solubility of water in hydrogen at high pressures: a molecular simulation study”. In: *Journal of Chemical & Engineering Data* 64.9 (2019), pp. 4103–4115.

[18] “The Future of Hydrogen”. en. In: ().

[19] Saša Polovina, Danijela Harmina, and Ana Granić Šarac. “HYDROGEN MANAGEMENT AT INA RIJEKA REFINERY”. In: *MOL GROUP SCIENTIFIC MAGAZINE 2013/2* (), p. 44.

[20] Ahmadreza Rahbari et al. “Effect of water content on thermodynamic properties of compressed hydrogen”. In: *Journal of Chemical & Engineering Data* 66.5 (2021), pp. 2071–2087.

[21] 14:00-17:00. *ISO 14687:2019*. en. URL: `https://www.iso.org/standard/69539.html` (visited on 01/25/2023).

[22] Shanhai Ge and Chao-Yang Wang. “Liquid water formation and transport in the PEFC anode”. In: *Journal of the Electrochemical Society* 154.10 (2007), B998.

[23] Bruno Belvedere et al. “Experimental analysis of a PEM fuel cell performance at variable load with anodic exhaust management optimization”. In: *international journal of hydrogen energy* 38.1 (2013), pp. 385–393.

[24] Philipp Haug, Matthias Koj, and Thomas Turek. “Influence of process conditions on gas purity in alkaline water electrolysis”. In: *International Journal of Hydrogen Energy* 42.15 (2017), pp. 9406–9418.

[25] P Trinke et al. “Hydrogen crossover in PEM and alkaline water electrolysis: mechanisms, direct comparison and mitigation strategies”. In: *Journal of The Electrochemical Society* 165.7 (2018), F502.

[26] Marcelo Carmo et al. “A comprehensive review on PEM water electrolysis”. In: *International journal of hydrogen energy* 38.12 (2013), pp. 4901–4934.

[27] Marian Chatenet et al. “Water electrolysis: from textbook knowledge to the latest scientific strategies and industrial developments”. In: *Chemical Society Reviews* (2022).

[28] Feng Ding and Boris I Yakobson. “Challenges in hydrogen adsorptions: from physisorption to chemisorption”. In: *Frontiers of Physics* 6.2 (2011), pp. 142–150.

[29] Taejun Kim et al. “A review of recent advances in hydrogen purification for selective removal of oxygen: Deoxo catalysts and reactor systems”. In: *International Journal of Hydrogen Energy* (2022).

[30] Yorick Ligen, Heron Vrubel, and Hubert Girault. “Energy efficient hydrogen drying and purification for fuel cell vehicles”. In: *International Journal of Hydrogen Energy* 45.18 (2020), pp. 10639–10647.

[31] Sang Ge et al. “Recombination of hydrogen and oxygen in fluidized bed reactor with different gas distributors”. In: *Energy Procedia* 29 (2012), pp. 552–558.

[32] E Lalik et al. “Humidity induced deactivation of Al2O3 and SiO2 supported Pd, Pt, Pd-Pt catalysts in H2+ O2 recombination reaction: The catalytic, microcalorimetric and DFT studies”. In: *Applied Catalysis A: General* 501 (2015), pp. 27–40.

[33] PM Gundry and FC Tompkins. “Chemisorption of gases on metals”. In: *Quarterly Reviews, Chemical Society* 14.3 (1960), pp. 257–291.

[34] Atanas Serbezov. “Adsorption equilibrium of water vapor on F-200 activated alumina”. In: *Journal of Chemical & Engineering Data* 48.2 (2003), pp. 421–425.

[35] Yu Wang. “Measurements and modeling of water adsorption isotherms of zeolite linde-type A crystals”. In: *Industrial & Engineering Chemistry Research* 59.17 (2020), pp. 8304–8314.

[36] Yu Wang and M Douglas LeVan. “Adsorption equilibrium of binary mixtures of carbon dioxide and water vapor on zeolites 5A and 13X”. In: *Journal of Chemical & Engineering Data* 55.9 (2010), pp. 3189–3195.

[37] Yu Wang and M Douglas LeVan. “Adsorption equilibrium of carbon dioxide and water vapor on zeolites 5A and 13X and silica gel: pure components”. In: *Journal of Chemical & Engineering Data* 54.10 (2009), pp. 2839–2844.

[38] M Van der Waarden and FEC Scheffer. “The adsorption of nitrogen, hydrogen and their mixtures on silica gel”. In: *Recueil des Travaux Chimiques des Pays-Bas* 71.7 (1952), pp. 689–698.

[39] María Yáñez et al. “PSA purification of waste hydrogen from ammonia plants to fuel cell grade”. In: *Separation and Purification Technology* 240 (2020), p. 116334.

[40] Alan L Myers and John M Prausnitz. “Thermodynamics of mixed-gas adsorption”. In: *AIChE journal* 11.1 (1965), pp. 121–127.

[41] Frederik Berg et al. “Temperature swing adsorption in natural gas processing: a concise overview”. In: *ChemBioEng Reviews* 6.3 (2019), pp. 59–71.

[42] Ayub Golmakani, Shohreh Fatemi, and Javad Tamnanloo. “Investigating PSA, VSA, and TSA methods in SMR unit of refineries for hydrogen production with fuel cell specification”. In: *Separation and Purification Technology* 176 (2017), pp. 73–91.

[43] Nan Jiang et al. “CO2 capture from dry flue gas by means of VPSA, TSA and TVSA”. In: *Journal of CO2 Utilization* 35 (2020), pp. 153–168.

[44] Ralph T Yang. *Gas separation by adsorption processes*. Vol. 1. World Scientific, 1997.

[45] Ana M Ribeiro et al. “A parametric study of layered bed PSA for hydrogen purification”. In: *Chemical Engineering Science* 63.21 (2008), pp. 5258–5273.

[46] Kent S Knaebel. “Adsorbent selection”. In: *Accessed on* 6.8 (2011).

[47] Arthur L Kohl and Richard B Nielsen. “Gas dehydration and purification by adsorption”. In: *Gas Purification* (1997), pp. 1022–1135.

[48] Douglas M Ruthven and FSKKS Pressure. “Swing adsorption”. In: *New York: VCH Publishers* 1.994 (1994), p. 235.

[49] Zhemin Du et al. “A review of hydrogen purification technologies for fuel cell vehicles”. In: *Catalysts* 11.3 (2021), p. 393.

[50] Si Huang et al. “Study on Liquid Ring Compressor Theoretical Model and Suction Compression Performance Based on the Actual Working Cycle”. In: *Journal of Chemical Engineering of Japan* 52.5 (2019), pp. 384–391.

[51] André B de Haan, H Burak Eral, and Boelo Schuur. “Industrial separation processes”. In: *Industrial Separation Processes*. De Gruyter, 2020.

[52] GE Keller, RA Anderson, and CM Yon. *Adsorption” inHandbook of Separation Technology*. 1987.

[53] Mohammad Saleh Shafeeyan, Wan Mohd Ashri Wan Daud, and Ahmad Shamiri. “A review of mathematical modeling of fixed-bed columns for carbon dioxide adsorption”. In: *Chemical engineering research and design* 92.5 (2014), pp. 961–988.

[54] Alan Gabelman. “Adsorption basics: part 1”. In: *Chemical Engineering Progress* 113.7 (2017), pp. 48–53.

[55] Józef Nastaj and Tomasz Aleksandrzak. “Adsorption isotherms of water, propan-2-ol, and methylbenzene vapors on grade 03 silica gel, sorbonorit 4 activated carbon, and HiSiv 3000 zeolite”. In: *Journal of Chemical & Engineering Data* 58.9 (2013), pp. 2629–2641.

[56] Mohammadreza Gaeini, Herbert A Zondag, and Camilo CM Rindt. “Non-isothermal kinetics of zeolite water vapor adsorption into a packed bed lab scale thermochemical reactor”. In: *International Heat Transfer Conference Digital Library*. Begel House Inc. 2014.

[57] J Prieur Du Plessis and Sonia Woudberg. “Pore-scale derivation of the Ergun equation to enhance its adaptability and generalization”. In: *Chemical Engineering Science* 63.9 (2008), pp. 2576–2586.

[58] Anthony F Mills and CFM Coimbra. *Basic heat transfer*. Temporal Publishing, LLC, 2015.

[59] AE Rodrigues, JM Loureiro, and MD LeVan. “Simulated pressurization of adsorption beds”. In: *Gas separation & purification* 5.2 (1991), pp. 115–124.

[60] F Benyahia and KE O’Neill. “Enhanced voidage correlations for packed beds of various particle shapes and sizes”. In: *Particulate science and technology* 23.2 (2005), pp. 169–177.

[61] Raj P Chhabra and Basavaraj Gurappa. *Coulson and Richardson’s chemical engineering: volume 2A: particulate systems and particle technology*. Butterworth-Heinemann, 2019.

[62] Narasimhan Sundaram and PC Wankat. “Pressure drop effects in the pressurization and blowdown steps of pressure swing adsorption”. In: *Chemical engineering science* 43.1 (1988), pp. 123–129.

[63] Abdon Atangana. *Fractional operators with constant and variable order with application to geohydrology*. Academic Press, 2017.

[64] Max Kandula. “On the effective thermal conductivity of porous packed beds with uniform spherical particles”. In: *Journal of Porous Media* 14.10 (2011).

[65] M Leva. “Fluid flow through packed beds”. In: *Chem. Eng* 56.5 (1949), pp. 115–117.

[66] Adrian Bejan. *Convection heat transfer*. John wiley & sons, 2013.

[67] Gordon Mckay. *Use of Adsorbents for the Removal of Pollutants from Wastewater*. CRC press, 1995.

[68] S Sircar and JR Hufton. “Why does the linear driving force model for adsorption kinetics work?” In: *Adsorption* 6 (2000), pp. 137–147.

[69] JJ Mahle and DK Friday. “In Axial Dispersion Effects on the Breakthrough Behavior of Favorably Adsorbed Vapors”. In: *Recents Progres en Genie Des Procedes, France, Meunier F, LeVan MD, Eds* (1991).

[70] Beverly E Avilés and M Douglas Levan. “Network models for nonuniform flow and adsorption in fixed beds”. In: *Chemical engineering science* 46.8 (1991), pp. 1935–1944.

[71] Bradley P Russell and M Douglas LeVan. “Nonlinear adsorption and hydrodynamic dispersion in self-similar networks”. In: *Chemical engineering science* 52.9 (1997), pp. 1501–1510.

[72] N Wakao and T Funazkri. “Effect of fluid dispersion coefficients on particle-to-fluid mass transfer coefficients in packed beds: correlation of Sherwood numbers”. In: *Chemical Engineering Science* 33.10 (1978), pp. 1375–1384.

[73] MF Edwards and JF Richardson. “Gas dispersion in packed beds”. In: *Chemical Engineering Science* 23.2 (1968), pp. 109–123.

[74] E Wicke. “Bedeutung der molekularen Diffusion für chromatographische Verfahren”. In: *Berichte der Bunsengesellschaft für physikalische Chemie* 77.3 (1973), pp. 160–171.

[75] Douglas M Ruthven. *Principles of adsorption and adsorption processes*. John Wiley & Sons, 1984.

[76] Chin-Yung Wen, Liang-tseng Fan, et al. *Models for flow systems and chemical reactors*. M. Dekker, 1975.

[77] FEng W John Thomas and Barry Crittenden. *Adsorption technology and design*. Butterworth-Heinemann, 1998.

[78] Mohsen Siahpoosh, Shohreh Fatemi, and Ali Vatani. “Mathematical modeling of single and multi-component adsorption fixed beds to rigorously predict the mass transfer zone and breakthrough curves”. In: *Iranian Journal of Chemistry and Chemical Engineering (IJCCE)* 28.3 (2009), pp. 25–44.

[79] Haripriya Naidu and Alexander P Mathews. “Linear driving force analysis of adsorption dynamics in stratified fixed-bed adsorbers”. In: *Separation and Purification Technology* 257 (2021), p. 117955.

[80] Stefano Brandani and Enzo Mangano. “Direct measurement of the mass transport coefficient of water in silica-gel using the zero length column technique”. In: *Energy* 239 (2022), p. 121945.

[81] James C Knox et al. “Limitations of breakthrough curve analysis in fixed-bed adsorption”. In: *Industrial & engineering chemistry research* 55.16 (2016), pp. 4734–4748.

[82] William E Schiesser. *The numerical method of lines: integration of partial differential equations*. Elsevier, 2012.

[83] John David Anderson and John Wendt. *Computational fluid dynamics*. Vol. 206. Springer, 1995.

[84] Python Software Foundation. *Python*. Accessed on Date. Year. URL: `https://www.python.org`.

[85] SciPy Community. *SciPy: Open Source Scientific Tools for Python*. Version 1.11.2. SciPy. 2023. URL: `https://docs.scipy.org/doc/scipy/reference/generated/scipy.integrate.solve_ivp.html`.

[86] Gerhard Wanner and Ernst Hairer. *Solving ordinary differential equations II*. Vol. 375. Springer Berlin Heidelberg New York, 1996.

[87] Carlos Sereno and Alírio Rodrigues. “Can steady-state momentum equations be used in modelling pressurization of adsorption beds?” In: *Gas separation & purification* 7.3 (1993), pp. 167–174.

[88] Oliver J Smith IV and Arthur W Westerberg. “The optimal design of pressure swing adsorption systems”. In: *Chemical engineering science* 46.12 (1991), pp. 2967–2976.

[89] Niels De Witte, Joeri FM Denayer, and Tom RC Van Assche. “Effect of adsorption duration and purge flowrate on pressure swing adsorption performance”. In: *Industrial & Engineering Chemistry Research* 60.37 (2021), pp. 13684–13691.

[90] Hantong Wang et al. “Research and demonstration on hydrogen compatibility of pipelines: a review of current status and challenges”. In: *International Journal of Hydrogen Energy* 47.66 (2022), pp. 28585–28604.

[91] Zhaoyang Ding et al. “Optimization and analysis of the VPSA process for industrial-scale oxygen production”. In: *Adsorption* 24 (2018), pp. 499–516.

[92] Jatupol Khunpolgrang et al. “Alternative PSA process cycle with combined vacuum regeneration and nitrogen purging for CH4/CO2 separation”. In: *Fuel* 140 (2015), pp. 171–177.

[93] Swapnil Divekar et al. “Recovery of hydrogen and carbon dioxide from hydrogen PSA tail gas by vacuum swing adsorption”. In: *Separation and Purification Technology* 254 (2021), p. 117113.

[94] Brian Joseph Maring and Paul A Webley. “A new simplified pressure/vacuum swing adsorption model for rapid adsorbent screening for CO2 capture applications”. In: *International Journal of Greenhouse Gas Control* 15 (2013), pp. 16–31.

[95] Reza Haghpanah et al. “Multiobjective optimization of a four-step adsorption process for post-combustion CO2 capture via finite volume simulation”. In: *Industrial & Engineering Chemistry Research* 52.11 (2013), pp. 4249–4265.

A

Derivations

A.1. Mass balance

The derivation of mass balance starts with the differential form of the Continuity equation in Fluid dynamics:

$$\frac{\partial \rho}{\partial t} + \frac{\partial (\rho u)}{\partial z} = 0 \tag{A.1}$$

The preceding equation is still valid if the concentration replaces the density.

$$\frac{\partial c}{\partial t} + \frac{\partial (cu)}{\partial z} = s \tag{A.2}$$

where s is a source/sink therm specific to the case of adsorption/desorption. Examining the units of concentration and velocity it can be understood that their multiplication represents the molar flux, j:

$$cu = \left[\frac{mol}{m^3}\frac{m}{s} = \frac{mol}{m^2 s}\right] = j \tag{A.3}$$

Then the equation A.2 can be rearranges as following:

$$\frac{\partial c}{\partial t} + \frac{\partial j}{\partial z} = s \tag{A.4}$$

The molar flux can be described in terms of advection and diffusion as follows:

$$j = cu - D_L \frac{\partial c}{\partial z} \tag{A.5}$$

where D_L is the diffusion coefficient. The combination of the equations A.4 and A.5 gives:

$$\frac{\partial c}{\partial t} + \frac{\partial cu}{\partial z} - D_L \frac{\partial^2 c}{\partial z^2} = s \tag{A.6}$$

The s is the source/sink term, which has the following from:

$$s = -\sum_{i=1}^{N_c} \frac{\partial q_i}{\partial t} \rho_s \tag{A.7}$$

The dimensional analysis of equation A.6 shows that the left-hand side and right-hand side of the equation have the same unit $\left[\frac{mol}{s \cdot m^3}\right]$. Both sides of the equation should be multiplied by volume to get from differential form to integral form. The left-hand side of the equation describes the flow and it should be multiplied by the fluid volume V_f, which is equal to void volume. Whereas the source term is related to the adsorbent, meaning it is multiplied by solid volume, V_s:

$$V_f \left(\frac{\partial c_i}{\partial t} + \frac{\partial (c_i u)}{\partial z} - D_L \frac{\partial^2 c_i}{\partial z^2} \right) = -V_s \sum_{i=1}^{N_c} \frac{\partial q_i}{\partial t} \rho_s \tag{A.8}$$

The fluid and solid volumes can be described in terms of bed volume and porosity:

$$V_f = V_{\text{void}} = \varepsilon V_{\text{bed}} \tag{A.9}$$

$$V_s = (1 - \varepsilon) V_{\text{bed}} \tag{A.10}$$

The final form of mass balance equation is obtained by incorporating equations A.9 and A.10 into equation A.8:

$$\frac{\partial c_i}{\partial t} + \frac{\partial (c_i u)}{\partial z} - D_L \frac{\partial^2 c_i}{\partial z^2} = -\frac{(1-\varepsilon)}{\varepsilon} \sum_{i=1}^{N_c} \frac{\partial q_i}{\partial t} \rho_s \tag{A.11}$$

A.2. Energy balance for gas phase. Immediate thermal equilibrium between gas and solid phases

According to the law of energy conservation, the following equation applies:

$$\dot{E} = \dot{U} + \dot{PE} + \dot{KE} \tag{A.12}$$

Assuming negligible potential energy ($\dot{PE}$) and kinetic energy ($\dot{KE}$), Equation A.12 simplifies to:

$$\dot{E} = \dot{U} \tag{A.13}$$

The rate of change of internal energy is defined through heat flow, as schematically shown in Figure A.1:

$$\frac{\partial U}{\partial t} = A_{\text{void}} \dot{q}_{\text{cond}}(z) - A_{\text{void}} \dot{q}_{\text{cond}}(z+\Delta z) + A_{\text{void}} \dot{q}_{\text{conv}}(z) - A_{\text{void}} \dot{q}_{\text{conv}}(z+\Delta z) - A_{\text{wall}}^{\text{in}} \dot{q}_{\text{wall}} + \sum_{i=1}^{N_c} \rho_s V_s \frac{\partial q_i}{\partial t} \Delta H_i \tag{A.14}$$

Here, $\dot{q}_{\text{cond}}$ and $\dot{q}_{\text{conv}}$ represent conduction and convection heat transfer within the fluid, while $\dot{q}_{\text{wall}}$ denotes heat transfer from the gas to the adsorption column wall.

The left-hand side of Equation A.13 can be described as:

$$\frac{\partial U}{\partial t} = \frac{\partial (m_f C_{p,f} T_f + m_s C_{p,s} T_s)}{\partial t} = \rho_f V_f C_{p,f} \frac{\partial T_f}{\partial t} + \rho_s V_s C_{p,s} \frac{\partial T_s}{\partial t} \tag{A.15}$$

The simplified energy balance assumes immediate thermal equilibrium between the gas and adsorbent, implying equal gas and solid temperatures:

$$\frac{\partial U}{\partial t} = \left[\rho_f V_f C_{p,f} + \rho_s V_s C_{p,s} \right] \frac{\partial T_f}{\partial t} \tag{A.16}$$

The fluid volume and solid volume in Equation A.16 can be expressed in terms of bed volume and porosity using Equations A.9 and A.10:

$$\frac{\partial U}{\partial t} = \varepsilon V_{\text{bed}} \left[\rho_f C_{p,f} + \left(\frac{1-\varepsilon}{\varepsilon} \right) \rho_s C_{p,s} \right] \frac{\partial T_f}{\partial t} \tag{A.17}$$

It’s worth noting that the factor in Equation A.16 can be rewritten as:

$$V_f = V_{\text{void}} = \varepsilon V_{\text{bed}} = A_{\text{void}} \Delta z \tag{A.18}$$

Combining Equations A.14, A.17, and A.18, we obtain:

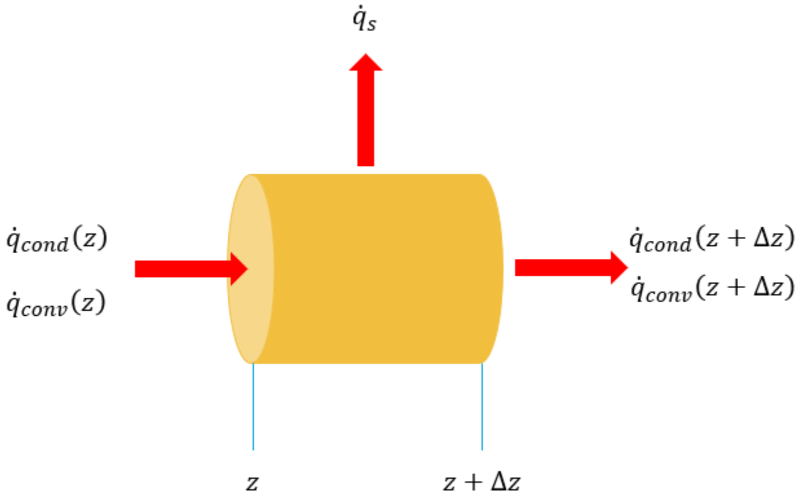

Figure A.1: Schematic drawing of heat flow

$$[\rho_f C_{p,f} + \rho_s C_{p,s}] \frac{\partial T_f}{\partial t} = -\frac{\dot{q}_{\text{cond}}(z+\Delta z) - \dot{q}_{\text{cond}}(z)}{\Delta z} - \frac{\dot{q}_{\text{conv}}(z+\Delta z) - \dot{q}_{\text{conv}}(z)}{\Delta z} - \frac{A^{\text{in}}_{\text{wall}}}{\varepsilon V_{\text{bed}}}\dot{q}_{\text{wall}} + \frac{V_s}{\varepsilon V_{\text{bed}}}\rho_s \sum_{i=1}^{N_c} \frac{\partial q_i}{\partial t}\Delta H_i \tag{A.19}$$

The first and second terms on the right-hand side of Equation A.19 represent derivatives of conduction and convection with respect to z:

$$[\rho_f C_{p,f} + \rho_s C_{p,s}] \frac{\partial T_f}{\partial t} = -\frac{\partial \dot{q}_{\text{cond}}}{\partial z} - \frac{\partial \dot{q}_{\text{conv}}}{\partial z} - \frac{A^{\text{in}}_{\text{wall}}}{\varepsilon V_{\text{bed}}}\dot{q}_w + \frac{V_s}{\varepsilon V_{\text{bed}}}\rho_s \sum_{i=1}^{N_c} \frac{\partial q_i}{\partial t}\Delta H_i \tag{A.20}$$

Inner wall surface area ($A^{\text{in}}_{\text{wall}}$) for cylindrical column is defined as follows:

$$A^{\text{in}}_{\text{wall}} = \pi d_{\text{in}} \Delta z \tag{A.21}$$

Equation A.20 can be simplified using definitions of inner wall surface area A.48 and solid volume A.10 :

$$[\rho_f C_{p,f} + \rho_s C_{p,s}] \frac{\partial T_f}{\partial t} = -\frac{\partial \dot{q}_{\text{cond}}}{\partial z} - \frac{\partial \dot{q}_{\text{conv}}}{\partial z} - \frac{4}{\varepsilon d_i}\dot{q}_{\text{wall}} + \rho_s \frac{1-\varepsilon}{\varepsilon} \sum_{i=1}^{N_c} \frac{\partial q_i}{\partial t}\Delta H_i \tag{A.22}$$

The expressions for conduction and convection in the fluid and heat transfer from the fluid to the wall are given by:

$$\dot{q}_{\text{cond}} = -k_f \frac{\partial T_f}{\partial z} \tag{A.23}$$

$$\dot{q}_{\text{conv}} = \rho_f u_f C_{p,f} T_f \tag{A.24}$$

$$\dot{q}_{\text{wall}} = h_w (T_f - T_w) \tag{A.25}$$

The change in fluid temperature with time, according to the simplified energy balance assumptions, is given by:

$$[\rho_f C_{p,f} + \rho_s C_{p,s}] \frac{\partial T_f}{\partial t} = k_f \frac{\partial^2 T_f}{\partial z^2} - \rho_f u_f C_{p,f} \frac{\partial T_f}{\partial z} - \frac{4}{\varepsilon d_{\text{in}}}\dot{q}_{\text{wall}} + \rho_s \frac{1-\varepsilon}{\varepsilon} \sum_{i=1}^{N_c} \frac{\partial q_i}{\partial t}\Delta H_i \tag{A.26}$$

A.3. Energy balance for gas phase

The energy balance for the gas phase starts with defining internal energy balance change:

$$\frac{\partial U_f}{\partial t} = \dot{q}_{\text{cond}}(z)A_{\text{void}} - \dot{q}_{\text{cond}}(z+\Delta z)A_{\text{void}} + \dot{q}_{\text{conv}}(z)A_{\text{void}} - \dot{q}_{\text{conv}}(z+\Delta z)A_{\text{void}} + \dot{q}_{\text{wall}}A_{\text{wall}}^{\text{in}} + \dot{q}_{\text{solid}}A_s \quad \text{(A.27)}$$

The right hand side of equation A.27 can be expanded as follows:

$$U_f = \dot{m}_f C_{p,f} T_f = \rho_f V_f C_{p,f} T_f \quad \text{(A.28)}$$

The combination of equations A.28 and A.18 result in:

$$U_f = \rho_f A_{\text{void}} \Delta z C_{p,f} T_f \quad \text{(A.29)}$$

Equation A.27 can be re-arranged using equation A.29:

$$\rho_f C_{p,f}\frac{\partial T_f}{\partial t} = -\frac{\dot{q}_{\text{cond}}(z+\Delta z) - \dot{q}_{\text{cond}}(z)}{\Delta z} - \frac{\dot{q}_{\text{conv}}(z+\Delta z) - \dot{q}_{\text{conv}}(z)}{\Delta z} - \frac{A_{\text{wall}}^{\text{in}}}{A_{\text{void}}\Delta z}\dot{q}_{\text{wall}} + \frac{A_{\text{s}}}{A_{\text{void}}\Delta z}\dot{q}_s \quad \text{(A.30)}$$

The first two terms in right hand side of equation A.30 are derivative of conduction and convection with respect to z:

$$\rho_f C_{p,f}\frac{\partial T_f}{\partial t} = -\frac{\partial \dot{q}_{\text{cond}}}{\partial z} - \frac{\partial \dot{q}_{\text{conv}}}{\partial z} - \frac{A_{\text{wall}}^{\text{in}}}{A_{\text{void}}\Delta z}\dot{q}_w + \frac{A_s}{A_{\text{void}}\Delta z}\dot{q}_{\text{solid}} \quad \text{(A.31)}$$

The void area (A_{void}) is derived from equation A.18 :

$$A_{\text{void}} = \frac{V_{\text{void}}}{\Delta z} \quad \text{(A.32)}$$

The solid area (A_s) is defined in approach similar to void area:

$$A_s = \frac{V_s}{\Delta z} \quad \text{(A.33)}$$

The facors in right hand side of equation A.31 can be simplified using equations A.32, A.33 and A.48:

$$\rho_f C_{p,f}\frac{\partial T_f}{\partial t} = -\frac{\partial \dot{q}_{\text{cond}}}{\partial z} - \frac{\partial \dot{q}_{\text{conv}}}{\partial z} - \frac{4}{\varepsilon d_{\text{in}}}\dot{q}_w + \frac{1-\varepsilon}{\varepsilon}\frac{1}{\Delta z}\dot{q}_{\text{solid}} \quad \text{(A.34)}$$

The convective heat transfer from solid to gas is defined as follows:

$$\dot{q}_s = h_f(T_s - T_f) \quad \text{(A.35)}$$

Equation A.34 can be further simplified using definitions of conduction A.23 and A.24 in the fluid, convective heat transfer from gas to wall A.25:

$$\rho_f C_{p,f}\frac{\partial T_f}{\partial t} = k_f\frac{\partial^2 T_f}{\partial z^2} - \rho_f u C_{p,f}\frac{\partial T_f}{\partial z} - \frac{4}{\varepsilon d_{\text{in}}}h_w(T_f - T_w) + \frac{1-\varepsilon}{\varepsilon}\frac{1}{\Delta z}h_f(T_s - T_f) \quad \text{(A.36)}$$

A.4. Energy balance for solid phase

The energy balance derivation for solid phase starts with defining internal energy change:

$$\frac{\partial U_s}{\partial t} = \dot{q}_{\text{cond}}(z)A_{\text{void}} - q_s A_s + q_{\text{source}}V_s \quad \text{(A.37)}$$

The internal energy for solid phase can be defined as follows:

$$U_s = \rho_s V_s C_{p,s} T_s = \rho_s A_s \Delta z C_{p,s} T_s \quad \text{(A.38)}$$

Equation A.37 can be rearranged using equation A.38:

$$\rho_s C_{p,s}\frac{\partial T_s}{\partial t} = -\frac{\dot{q}_{\text{cond}}(z+\Delta z) - \dot{q}_{\text{cond}}(z)}{\Delta z} - \frac{A_s}{V_s}\dot{q}_s + \dot{q}_{\text{source}} \tag{A.39}$$

The first term in right hand side of equation A.39 represents conductive heat transfer derivative with respect to z:

$$\rho_s C_{p,s}\frac{\partial T_s}{\partial t} = -\frac{\partial \dot{q}_{\text{cond}}}{\partial z} - \frac{A_s}{V_s}\dot{q}_s + \dot{q}_{\text{source}} \tag{A.40}$$

The solid volume (V_s) can be defined in terms of solid area (A_s) as:

$$V_s = A_s \Delta z \tag{A.41}$$

The combination of equations A.40 and A.41 result in:

$$\rho_s C_{p,s}\frac{\partial T_s}{\partial t} = -\frac{\partial \dot{q}_{\text{cond}}}{\partial z} - \frac{1}{\Delta z}\dot{q}_s + \dot{q}_{\text{source}} \tag{A.42}$$

The conductive heat transfer in the solid ($\dot{q}_{\text{cond}}$) and heat source ($\dot{q}_{\text{source}}$) are defined as follows:

$$\dot{q}_{\text{cond}} = -k_s\frac{\partial^2 T_s}{\partial z^2} \tag{A.43}$$

$$\dot{q}_{\text{source}} = \sum_{i=1}^{N_c}\frac{\partial q_i}{\partial t}\rho_s \Delta H_i \tag{A.44}$$

The final form of equation A.45 can be obtained by using equations A.35, A.43 and A.44:

$$\rho_s C_{p,s}\frac{\partial T_s}{\partial t} = k_s\frac{\partial^2 T_s}{\partial z^2} - \frac{1}{\Delta z}h_f(T_s - T_f) + \sum_{i=1}^{N_c}\frac{\partial q_i}{\partial t}\rho_s \Delta H_i \tag{A.45}$$

A.5. Energy balance for column wall

The change of column wall internal energy with time is defined as:

$$\frac{\partial U_w}{\partial t} = A_{\text{wall, c}}\dot{q}_{\text{cond}}(z) - A_{\text{wall, c}}\dot{q}_{\text{cond}}(z+\Delta z) + A^{\text{in}}_{\text{wall}}\dot{q}^{\text{in}}_{\text{conv}} - A^{\text{out}}_{\text{wall}}\dot{q}^{\text{out}}_{\text{conv}} \tag{A.46}$$

where $A_{\text{wall, c}}$ is cross-section area, whereas $A^{\text{in}}_{\text{wall}}$ and $A^{\text{out}}_{\text{wall}}$ denote the inner and outer column wall surface areas respectively:

$$A_{\text{wall, c}} = \frac{\pi}{4}(d^2_{\text{out}} - d^2_{\text{in}}) \tag{A.47}$$

$$A^{\text{in}}_{\text{wall}} = \pi d_{\text{in}}\Delta z \tag{A.48}$$

$$A^{\text{out}}_{\text{wall}} = \pi d_{\text{out}}\Delta z \tag{A.49}$$

The left side of the equation can be expanded in the following way:

$$\frac{\partial U_w}{\partial t} = \rho_w V_w C_{p,w}\frac{\partial T_w}{\partial t} \tag{A.50}$$

where V_w is a column wall volume, which is defined as:

$$V_w = A_{\text{wall, c}}\Delta z \tag{A.51}$$

Equation A.50 can be rearranged using A.51:

$$\frac{\partial U_w}{\partial t} = \rho_w A_{\text{wall, c}}\Delta z C_{p,w}\frac{\partial T_w}{\partial t} \tag{A.52}$$

The combination of Equations A.46, A.48, A.49 and A.52 result in:

$$\rho_w C_{p,w}\frac{\partial T_w}{\partial t} = -\frac{\dot{q}_{\text{cond}}(z+\Delta z) - \dot{q}_{\text{cond}}(z)}{\Delta z} + \frac{\pi d_{\text{in}}}{A_{\text{wall, c}}}\dot{q}^{\text{in}}_{\text{conv}} - \frac{\pi d_{\text{out}}}{A_{\text{wall, c}}}\dot{q}^{\text{out}}_{\text{conv}} \tag{A.53}$$

The first term on the right-hand side of Equation A.53 represents the derivative of conduction with respect to z:

$$\rho_w C_{p,w}\frac{\partial T_w}{\partial t} = -\frac{\partial \dot{q}_{\text{cond}}}{\partial z} + \frac{\pi d_{\text{in}}}{A_{\text{wall, c}}}\dot{q}^{\text{in}}_{\text{conv}} - \frac{\pi d_{\text{out}}}{A_{\text{wall, c}}}\dot{q}^{\text{out}}_{\text{conv}} \tag{A.54}$$

where $\dot{q}_{\text{cond}}$ is conduction in the wall, whereas $\dot{q}^{\text{in}}_{\text{conv}}$ is convective heat transfer from fluid to inner wall surface and $\dot{q}^{\text{out}}_{\text{conv}}$ is convective heat transfer from outer wall surface to environment:

$$\dot{q}_{\text{cond}} = -k_w\frac{\partial T_w}{\partial z} \tag{A.55}$$

$$\dot{q}^{\text{in}}_{\text{conv}} = \dot{q}_{\text{wall}} = h_w(T_f - T_w) \tag{A.56}$$

$$\dot{q}^{\text{out}}_{\text{conv}} = h_\infty(T_w - T_e) \tag{A.57}$$

The wall temperature change with time is obtained by combining Equations A.47, A.54, A.55, A.56 and A.57 result in:

$$\rho_w C_{p,w}\frac{\partial T_w}{\partial t} = k_w\frac{\partial^2 T_w}{\partial z^2} + \frac{4d_{\text{in}}}{(d^2_{\text{out}} - d^2_{\text{in}})}h_w(T_f - T_w) - \frac{4d_{\text{out}}}{(d^2_{\text{out}} - d^2_{\text{in}})}h_\infty(T_w - T_e) \tag{A.58}$$

The outer diameter can be described in terms of inner diameter and wall thickness:

$$d_{\text{out}} = d_{\text{in}} + t_w \tag{A.59}$$

The Equation A.59 combined with A.58 gives:

$$\rho_w C_{p,w}\frac{\partial T_w}{\partial t} = k_w\frac{\partial^2 T_w}{\partial z^2} + \frac{4d_{\text{in}}}{(d_{\text{in}} + t_w)^2 - d^2_{\text{in}}}h_w(T_f - T_w) - \frac{4(d_{\text{in}} + t_w)}{(d_{\text{in}} + t_w)^2 - d^2_{\text{in}}}h_\infty(T_w - T_e) \tag{A.60}$$

A.6. Pressurization with an inert gas

The derivation pressure change in time and space domains starts with expanding the Continuity equation A.1:

$$\frac{\partial \rho}{\partial t} = -u\frac{\partial \rho}{\partial z} - \rho\frac{\partial u}{\partial z} \tag{A.61}$$

The density can be expressed in terms of the pressure using the Ideal gas law:

$$\rho = P\frac{M}{RT} \tag{A.62}$$

Then equation A.61 can be rearranged using the equation A.62 and isothermal bed assumption in the following way:

$$\frac{M}{RT}\frac{\partial P}{\partial t} = -u\frac{M}{RT}\frac{\partial P}{\partial z} - \frac{M}{RT}P\frac{\partial u}{\partial z} \tag{A.63}$$

Equation A.63 is simplified by cancelling out the common factor in left and right hand side of the equation:

$$\frac{\partial P}{\partial t} = -u\frac{\partial P}{\partial z} - P\frac{\partial u}{\partial z} \tag{A.64}$$

A.7. Pressurization with a binary mixture of inert and adsorbable gases

Modelling pressurisation of an adsorption bed with a binary mixture of inert gas and active gas starts with defining mass balance for both components:

$$\frac{\partial c_1}{\partial t} = \frac{\partial}{\partial z}\left[D_L c \frac{\partial y_1}{\partial z} - c_1 u\right] - \left(\frac{1-\epsilon}{\epsilon}\right)\rho_s \frac{\partial q}{\partial t} \tag{A.65}$$

$$\frac{\partial c_2}{\partial t} = \frac{\partial}{\partial z}\left[D_L c \frac{\partial y_2}{\partial z} - c_2 u\right] \tag{A.66}$$

where 1 and 2 stand for active and inert gases respectively. The total concentration and concentration for each species can be defined using the Ideal gas law:

$$c = \frac{P}{RT} \tag{A.67}$$

$$c_i = \frac{P_i}{RT} = \frac{y_i P}{RT} \tag{A.68}$$

The mass balance equations for each species can be rearranged by introducing the Ideal gas law:

$$P\frac{\partial y_1}{\partial t} + y_1\frac{\partial P}{\partial t} = D_L\left(P\frac{\partial^2 y_1}{\partial z^2} + \frac{\partial y_1}{\partial z}\frac{\partial P}{\partial z}\right) - u\left(P\frac{\partial y_1}{\partial z} + y_1\frac{\partial P}{\partial z}\right) - y_1 P\frac{\partial u}{\partial z} - \left(\frac{1-\epsilon}{\epsilon}\right)\rho_s\frac{\partial q}{\partial t}RT \tag{A.69}$$

$$P\frac{\partial y_2}{\partial t} + y_2\frac{\partial P}{\partial t} = D_L\left(P\frac{\partial^2 y_2}{\partial z^2} + \frac{\partial y_2}{\partial z}\frac{\partial P}{\partial z}\right) - u\left(P\frac{\partial y_2}{\partial z} + y_2\frac{\partial P}{\partial z}\right) - y_2 P\frac{\partial u}{\partial z} \tag{A.70}$$

The relationship between active and inert gases is given as:

$$y_2 = 1 - y_1 \tag{A.71}$$

Equation A.70 can be described in terms of active gas using Equation A.71:

$$-P\frac{\partial y_1}{\partial t} + (1-y_1)\frac{\partial P}{\partial t} = D_L\left(-P\frac{\partial^2 y_1}{\partial z^2} - \frac{\partial y_1}{\partial z}\frac{\partial P}{\partial z}\right) - u\left(-P\frac{\partial y_1}{\partial z} + (1-y_1)\frac{\partial P}{\partial z}\right) - (1-y_1)P\frac{\partial u}{\partial z} \tag{A.72}$$

The sum of Equations A.69 and A.72 result in:

$$\frac{\partial P}{\partial t} = -u\frac{\partial P}{\partial z} - P\frac{\partial u}{\partial z} - \frac{1-\varepsilon}{\varepsilon}RT\frac{\partial q}{\partial t}\rho_s \tag{A.73}$$

The combination of Equations A.70 and A.73 result in:

$$\frac{\partial y_1}{\partial t} = D_L\left(P\frac{\partial^2 y_1}{\partial z^2} - \frac{1}{P}\frac{\partial y_1}{\partial z}\frac{\partial P}{\partial z}\right) - u\frac{\partial y_1}{\partial z} - \frac{1-\varepsilon}{\varepsilon}\rho_s\frac{\partial q}{\partial t}\frac{(1-y_1)RT}{P} \tag{A.74}$$